Soft Microfluidic Assemblies of Sensors, Circuits, and Radios for the Skin

Sheng Xu *et al.*

Science **344**, 70 (2014);
DOI: 10.1126/science.1250169

Soft Microfluidic Assemblies of Sensors, Circuits, and Radios for the Skin

Sheng Xu,[1]* Yihui Zhang,[2,3]* Lin Jia,[1]* Kyle E. Mathewson,[4]* Kyung-In Jang,[1] Jeonghyun Kim,[1,6] Haoran Fu,[2,5] Xian Huang,[1] Pranav Chava,[1] Renhan Wang,[1] Sanat Bhole,[1] Lizhe Wang,[1] Yoon Joo Na,[1] Yue Guan,[1] Matthew Flavin,[1] Zheshen Han,[1] Yonggang Huang,[2]† John A. Rogers[1,4]†

When mounted on the skin, modern sensors, circuits, radios, and power supply systems have the potential to provide clinical-quality health monitoring capabilities for continuous use, beyond the confines of traditional hospital or laboratory facilities. The most well-developed component technologies are, however, broadly available only in hard, planar formats. As a result, existing options in system design are unable to effectively accommodate integration with the soft, textured, curvilinear, and time-dynamic surfaces of the skin. Here, we describe experimental and theoretical approaches for using ideas in soft microfluidics, structured adhesive surfaces, and controlled mechanical buckling to achieve ultralow modulus, highly stretchable systems that incorporate assemblies of high-modulus, rigid, state-of-the-art functional elements. The outcome is a thin, conformable device technology that can softly laminate onto the surface of the skin to enable advanced, multifunctional operation for physiological monitoring in a wireless mode.

Continuous physiological monitoring and intervention are needed for the treatment of many medical conditions. Multimodal, noninvasive access to the body can be accomplished through cutaneous electrical/optical/fluidic interfaces. "Skin-like" devices, sometimes referred to as "epidermal" electronic systems (*1*, *2*), offer thicknesses (*3*–*5*), moduli, levels of elastic stretchability, and other basic physical properties that match those of the skin itself so as to allow a soft, compliant type of integration. Recent work demonstrates that such characteristics can be achieved by exploiting ultrathin geometries (*1*, *6*, *7*), soft active materials (*3*, *4*, *8*–*13*), and/or liquid metals (*14*–*16*). Here, we demonstrate ideas that expand options beyond these specialized approaches to include commercial, chip-scale components, ranging from integrated circuits, to radio frequency hardware, microelectromechanical structures, physical/chemical sensors, and power sources. The key concept involves microfluidic suspensions of interconnected assemblies of such chips in thin elastomeric enclosures to enable soft, low-modulus mechanics at the system level. Here, the high-modulus components have little impact on the overall mechanics, even when they are present at high areal coverage. For otherwise similar device layouts, this strategy improves the mechanical compliance and the stretchability by orders of magnitude compared with those possible using previous approaches that incorporate chip-scale components (*17*–*20*). The resulting systems can laminate softly and noninvasively onto the skin to define highly functional interfaces with the ability to combine unusual elements with standard parts. These concepts enable broad classes of sophisticated bio-integrated electronic devices, as illustrated here through systems that offer wirelessly powered operation and precision measurement of biopotentials, acceleration, and/or temperature, with radio frequency (RF) data transmission.

The layout involves a matrix of microfluidic spaces designed to decouple the mechanics of the constituent devices and associated interconnect network from a thin, elastomeric enclosure that simultaneously provides a supporting surface (substrate) and an encapsulation layer (superstrate). Each component selectively bonds to the bottom surface of this enclosure at small, localized cylindrical features of relief (support posts) molded onto the thin elastomer substrate. Except for these posts, the devices are suspended in the surrounding fluid and, as a result, are mechanically isolated. A free-floating network of serpentine-shaped interconnects with multilayer, neutral mechanical plane layouts joins the devices into circuit architectures that provide system-level function. Presented in Fig. 1A is an exploded view schematic illustration of an integrated device capable of acquisition, filtering, amplification, and RF transmission of electrophysiological (EP) data, for precision measurement of electrocardiograms (ECGs), electromyograms (EMGs), electrooculograms (EOGs), and electroencephalograms (EEGs).

Bonding the superstrate and substrate at their edges defines a microfluidic structure that is subsequently filled with a dielectric fluid by use of an injection needle (Fig. 1B and fig. S1). Selection criteria for the fluid include (i) wettability toward the electronic components and the substrate/superstrate to facilitate the filling process, (ii) large volume resistivity ($>1 \times 10^{14}$ Ohm · cm) to eliminate electrical crosstalk, (iii) high dielectric strength (>10 kV/mm) to avoid electrical breakdown, (iv) moderate viscosity (~5 Pa · s) to enhance impact resistance, (v) good thermal stability [weight loss < 0.5% at 100°C for 4 hours (fig. S2)] to allow reliable long-term operation, (vi) low-loss RF properties and small dielectric constant (<3) to minimize influence on RF operation, (vii) low reactivity and chemical stability to avoid corrosion or other forms of chemical degradation, (viii) hydrophobic character to expel moisture from the package, and (ix) optical transparency to enable rapid inspection of the components. The devices reported here use a soft, silicone elastomer (Ecoflex, Smooth-On, Easton, Pennsylvania) for the substrate/superstrate, and a high-molecular-weight silicone oligomer (Sylgard 184, without curing agent) for the fluid.

The free-floating interconnects can buckle, twist, and deform with little constraint, both in and out of the plane, in response to externally imposed deformations of the entire system. Likewise, the fluid-based strain isolation strategy allows large-range motions of the substrate/superstrate with minimal coupling to the device components. This mechanics are apparent from the three-dimensional (3D) finite element analysis (FEA) results of Fig. 1C. The ability of the interconnects to move freely increases their range of stretchability, relative to designs that involve bonding to or embedding in solid or porous elastomers (*17*–*23*). For the case of an interconnect shown in Fig. 1C, this increase in stretchability corresponds to a factor of ~10 or ~20 when compared with the case of bonding or embedding, respectively (fig. S3). The maximum principal strain in the interconnect metal (Fig. 1C) is less than ~0.2% for a biaxial stretch of 50% for the entire system. The support posts lead to differences in absolute strains between the hard components and the elastomer immediately below, which can be as large as ~64% for the same level (50%) of biaxial stretch.

A dense array of sharp, pyramidal features molded onto the substrate prevent nonspecific adhesion to the interconnects and the devices, to allow low-friction, lubricated relative motions. The cross-sectional scanning electron microscope (SEM) images of Fig. 1D and fig. S4 show this relief, as well as that associated with a support post to allow strain isolation of component chips

[1]Department of Materials Science and Engineering and Frederick Seitz Materials Research Laboratory, University of Illinois at Urbana-Champaign, Urbana, IL 61801, USA. [2]Department of Mechanical Engineering and Department of Civil and Environmental Engineering, Center for Engineering and Health, and Skin Disease Research Center, Northwestern University, Evanston, IL 60208, USA. [3]Center for Mechanics and Materials, Tsinghua University, Beijing, 100084, P.R. China. [4]Beckman Institute for Advanced Science and Technology, University of Illinois at Urbana-Champaign, Urbana, IL 61801, USA. [5]Department of Civil Engineering and Architecture, Zhejiang University, Hangzhou 310058, P.R. China. [6]Department of Materials Science and Engineering, Department of Energy Engineering, Hanyang University, Seoul 133-791, Republic of Korea.

*These authors contributed equally to this work.
†Corresponding author. E-mail: jrogers@illinois.edu (J.A.R.); y-huang@northwestern.edu (Y.H.)

and a physical barrier to prevent entanglement of adjacent interconnects. The same region after integration of the interconnect network by transfer printing appears in Fig. 1, E and F. The chips [all <1 mm in thickness, achieved with mechanical grinding (fig. S5)] bond electrically and mechanically to this network via a low-temperature solder (figs. S6 and S7 and movie S1). Wide, straight traces (fig. S8) pass through opposite edges of the microfluidic enclosure (microfluidic thickness, ~1 mm; superstrate thickness, ~0.1 mm) and terminate at external contact pads that provide locations for lamination of epidermal electrodes (fig. S9) as interfaces to the skin. The completed system (Fig. 1G) includes modules for (i) wireless power supply through resonant inductive energy transfer, (ii) low-noise amplification and filtering of EP signals, and (iii) frequency-modulated RF transmission of measured data. The components and the design rationale are summarized in table S1 and fig. S10. The abilities of the device to stretch (shown here to ~30% uniaxial strain) and twist (shown here to ~75°) are evident from images in Fig. 1, H and I, respectively. Details on the materials and fabrication procedures are available as supplementary materials on *Science* Online.

Mechanical behaviors at the system level are important to overall design. Summarized in Fig. 2 are systematic computational and experimental studies of the device in Fig. 1, without the superstrate membrane to facilitate imaging. 3D-FEA results (Fig. 2A) and experimental pictures (Fig. 2B) reveal the configurations of the chips and interconnects at various levels of equal-biaxial stretch. The good agreement validates the models

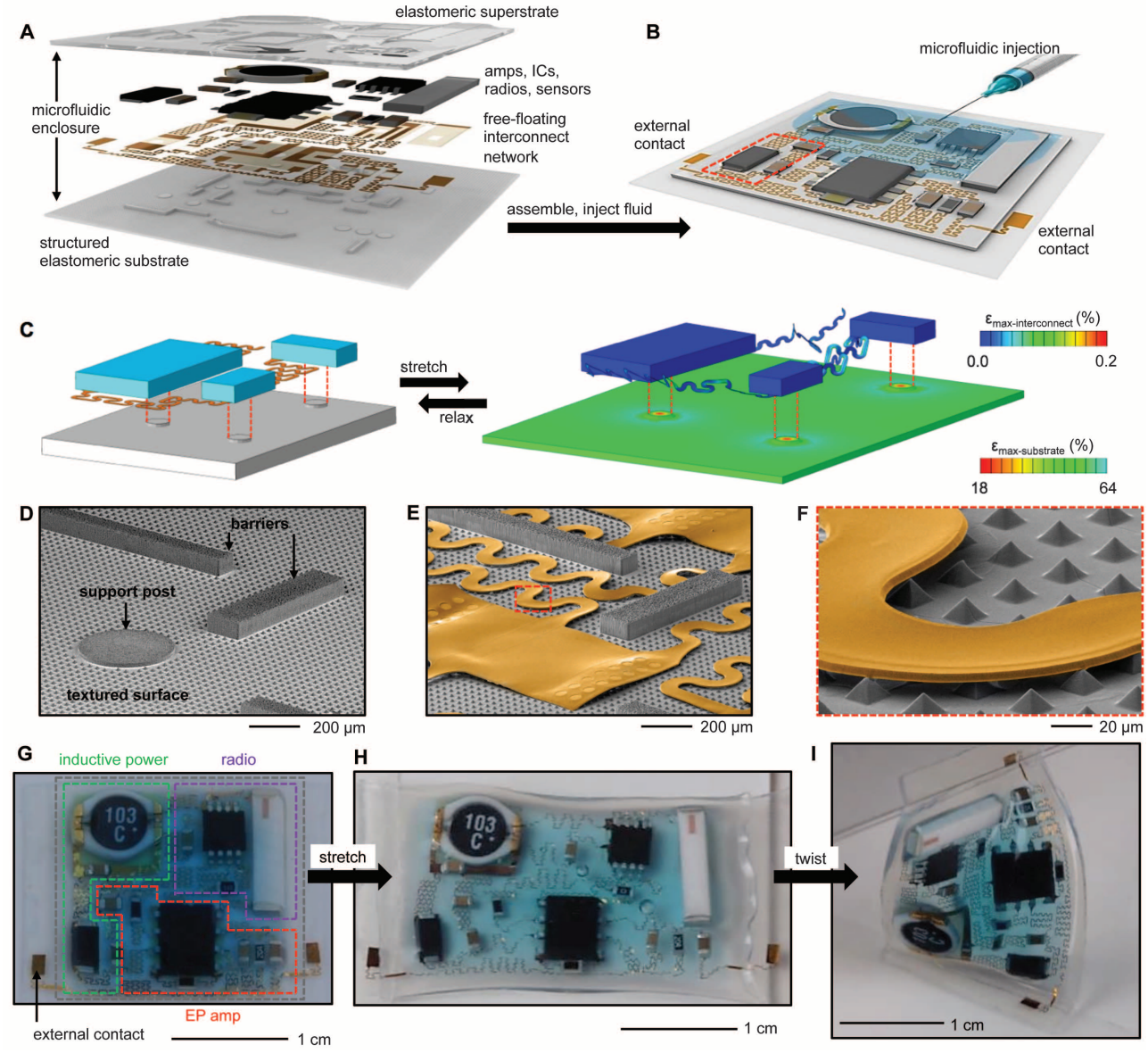

Fig. 1. Schematic illustrations, SEMs, and pictures of a soft, stretchable electronic system that integrates strain-isolated device components and a free-floating interconnect network in a thin elastomeric microfluidic enclosure. (**A**) Exploded-view schematic illustration of the key components of the system. (**B**) Illustration of the system after assembly, during initial stages of microfluidic injection using a syringe. (**C**) 3D-FEA results, in exploded-view format, that show the mechanics associated with equal-biaxial stretching of a small region of this system, as indicated by the red dash box in (B). The colors indicate the maximum principal strains. The buckling physics of the free-floating serpentine interconnects and the strain isolation mechanics of the suspended chips represent the key features. (**D**) Angled-view SEM of a region of the substrate showing a textured surface with different structures labeled. (**E**) Angled-view SEM of the same region in (D), after transfer printing the interconnect network (yellow). (**F**) Angled-view SEM of the region of (E) indicated by the red dashed box. (**G**) Image of a system with the colored dashed boxes and labels to identify the various subsystems. The gray dashed box around the periphery indicates, approximately, the location of bonding of the superstrate. (**H** and **I**) Image of this system in a (H) stretched and (I) twisted configuration.

and establishes their utility as design tools for optimizing the layouts of the chips and the shapes of the interconnects. In particular, for any choice of system geometry the computed results allow rapid identification of locations of (i) high principal strains, (ii) entanglements in the interconnects, and (iii) collisions between the chips. An iterative process that involves coupled considerations in circuit and mechanics design, with 3D-FEA modeling as a guide, allows optimization of all relevant parameters (including positions of molded barriers) for a desired device size, degree of stretchability, and effective modulus. The system shown here results from several iterations in the layouts of the chips and the geometries of the self-similar serpentine shapes that form the aperiodic interconnection network. Attention to the hierarchical mechanics of in- and out-of-plane bending and twisting in the serpentines and their dependence on geometry is paramount, subject to constraints set by requirements on their electrical properties. The subtle effects that can occur are shown in Fig. 2C and fig. S11. An example of one of the many modifications introduced with guidance from theory is a small bonding site added at the midpoint of the long interconnect at the base edge so as to ensure reversibility in its mechanics and to avoid entanglements (fig. S7). The final design offers an effective modulus, at the system level, that is only slightly larger (by 3 to 5%) than the intrinsic value associated with the bare elastomeric substrate (table S2). Uniaxial testing of the substrate with and without the chips, interconnect network, and surrounding fluid reveal almost identical stress/strain responses, as shown in the bottom frame of Fig. 2B. This outcome is notable, considering the large differences between the moduli of the electronic materials (~100 GPa) and the elastomers (~180 kPa).

In addition to a low modulus, the system offers a large range of stretchability. For example, 100% equal-biaxial strain induces maximum principal strains of only ~2% in the active materials (Cu of the interconnects), as highlighted by a segment of the interconnect network shown in the bottom frame of Fig. 2A. The maximum biaxial stretchability predicted with 3D-FEA is ~125%, limited by localized fracture of the Cu (failure strain ~5%) in the interconnect network, which is consistent with experimental observation (~100%). Reversible, elastic behaviors can be obtained (yield strain of Cu, ~0.3%) for biaxial strains of ~49% (fig. S12), even with the high (~46%) cumulative areal coverage of chips

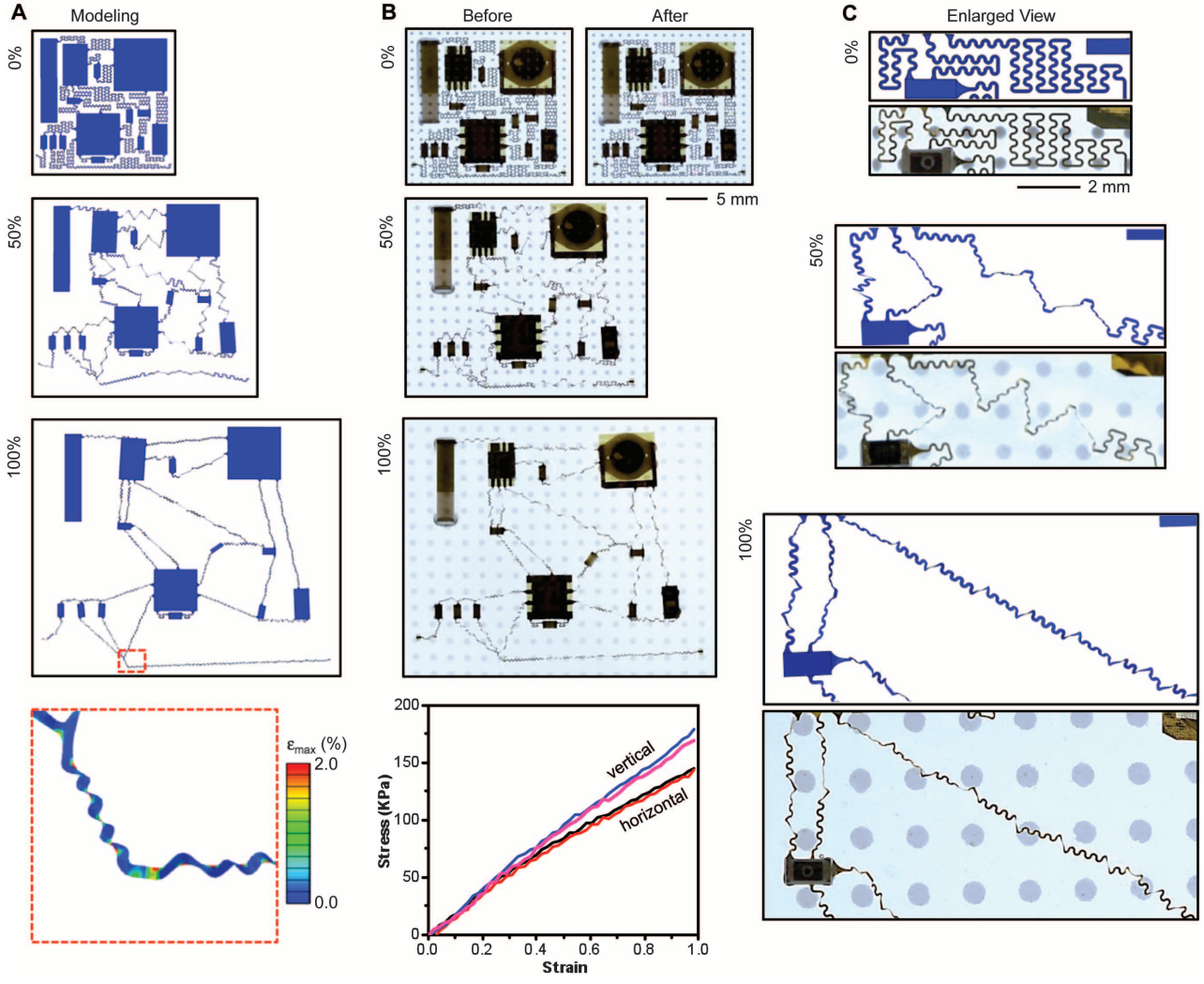

Fig. 2. Computational and experimental studies of the physics of buckling in free-floating interconnect networks and of strain isolation in suspended chips for a wireless EP sensor. (**A**) System-level 3D-FEA results for various magnitudes of equal-biaxial tensile strain. The color shows the maximum principal strains across each part of the system. (Bottom) Illustration of a small region of the interconnect network. (**B**) Optical images of the device at equal-biaxial strains that correspond to those evaluated by 3D-FEA. An additional image shows the system after release of the strain, to illustrate reversibility in the responses. (Bottom) Graph of the stress/strain responses measured by uniaxial testing for the case of a system with (black, in horizontal; blue, in vertical) and without (red, in horizontal; pink, in vertical) the chips and interconnect network. The results indicate nearly complete decoupling of the mechanics of the chips and interconnects from the substrate. (**C**) Images and 3D-FEA results for a local region.

in this device layout. Practical limits in uniaxial stretching are ~40%, defined by collisions of adjacent chips caused by orthogonal contractions that arise from the Poisson effect (figs. S13 and S14). The device can be cycled for more than 6000 times under 30% uniaxial strain at a frequency of 0.6 Hz (fig. S15) without degradation. In all cases, deformations in the substrate show no evidence of constraints in motion associated with the chips or the interconnect network, as illustrated by the uniform separations between fiducial dots (Cr, 100 nm thick) deposited in a square array on the back surface of the substrate, which is visible in the images of Fig. 2. Quantitative analysis is provided in fig. S16. This low-modulus [~180 kPa, as soft as the skin (*1*)], isotropic stretchable response follows from the microfluidic strain-isolation approaches. Analogous systems that do not exploit selective bonding of the chips to support posts show highly nonuniform deformations in the substrate (fig. S17); those that replace the microfluidics with solid elastomer show an elastic stretchability of only 6% and local effective moduli that vary from values comparable with those of the chips themselves (>100 GPa) to the elastomer constrained by the bonded interconnects (~250 kPa). Such characteristics are poorly matched to requirements for mounting on the skin.

Shown in Fig. 3, A and B, is a completed device (~1.7 × 1.8 cm^2) that includes a pair of epidermal electrodes (each ~0.8 × 1 cm^2, in fila-

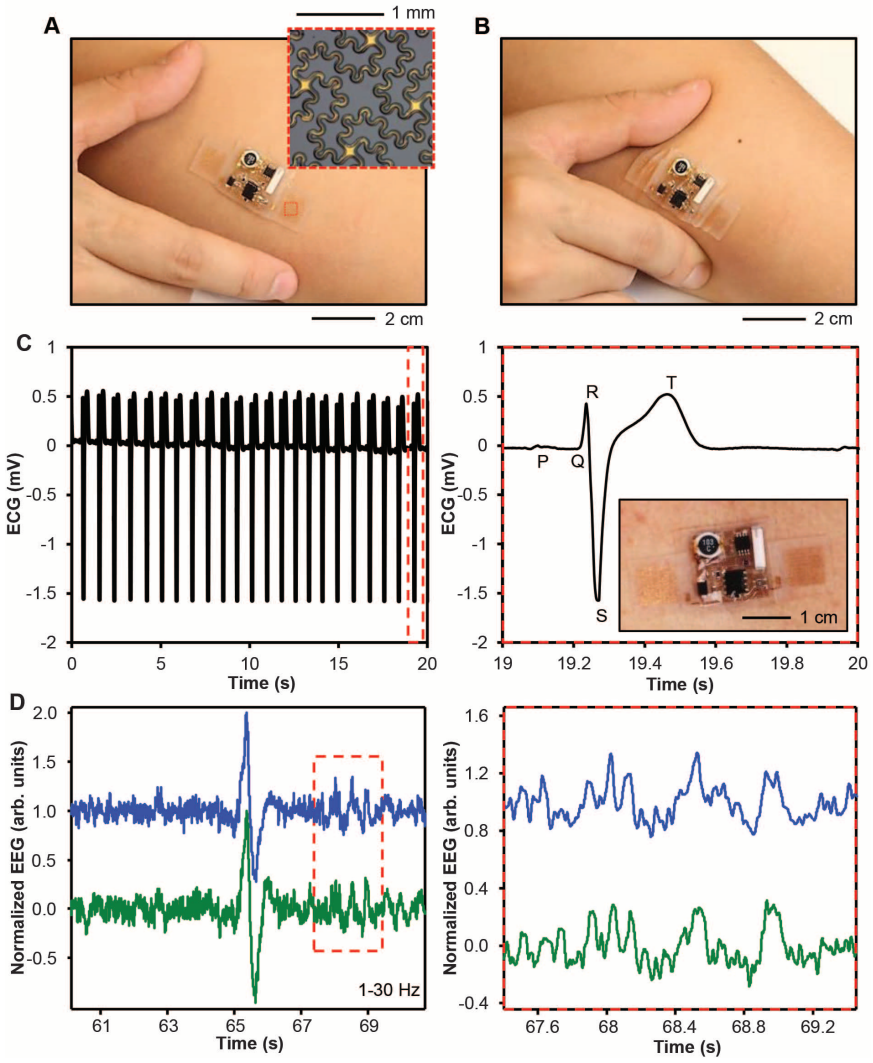

Fig. 3. Images and operational data from a wireless EP sensor. (**A** and **B**) Optical images of the device on the forearm, with a pair of epidermal electrodes in self-similar serpentine mesh layouts (inset optical micrograph) for an (A) undeformed state and (B) compressed and twisted state. (**C**) ECG acquired by using a device mounted on the sternum. The graph on the right provides a detailed view that shows the expected Q, R, and S waveforms. (**D**) EEG acquired from the left forehead during mental math and rest (green), and simultaneous measurement by using a wired commercial device (blue), mounted next to the wireless system. The large deflection represents the eyes closing as the subject shifts from mental math to resting, as shown in detail in the right plot. Data are plotted in arbitrary units, normalized and offset in the vertical direction to facilitate comparisons.

mentary, self-similar serpentine mesh designs) (fig. S18) laminated onto the skin of the forearm, in undeformed and deformed states, respectively. Here, low interface stresses associated with the low effective modulus of the device enable robust adhesion to the skin through van der Waals forces alone, facilitated by an ultralow modulus thin elastomer coating on the bottom surface of the substrate. Alternating voltage (150 kHz) applied to a primary coil in proximity (within millimeters) to the device activates it by creating direct current output from the inductive power module. The total power consumption is ~35 mW. Laminating the device across the sternum with the electrodes in bilateral fourth intercostal spaces enables wireless (~2.4 GHz) collection of ECG (movie S2) at distances of up to 1 m (fig. S19). The data show excellent signal-to-noise ratios, with clearly identifiable sequences of Q, R, and S waveforms (Fig. 3C). The fidelity of this system is similar to that of conventional commercial hardware with wired connections (fig. S20). Even weak electrophysiological signals can be captured effectively through EEG measured between electrodes on the forehead (positions Fpz and AF7), as illustrated in Fig. 3D, compared with signals simultaneously collected by using commercial hardware. Here, the subject engaged in mental math (counting backward by 7 from 200) for 1 min, closed his eyes, and remained at rest for another minute. EOG activity from the eyes closing separates the two tasks. The data reveal strong high-frequency activity during mental math and strong low-frequency activity during rest (fig. S21), as expected. Experimental details and many additional examples (fig. S22) appear in the supplementary materials.

The core concepts can also be used in multifunctional systems that allow not only EP sensing but also precision recording of motion with a triaxial accelerometer and with a thermal sensor, switched sequentially by a multiplexer (fig. S23). Such capabilities are important for applications that range from training in sports to tracking in sleep apnea studies, monitoring in neonatal care, and assessing cognitive state and awareness. The device in this case (1.9 × 2.9 cm^2) includes 31 component chips and a complex, multilayer interconnect network. The components and design rationale are summarized in table S3 and fig. S24. At low duty cycle operation (fig. S25), the power consumption (few milliwatts) lies in a range that can be addressed not only with near-field communication, but also with a small coin-cell battery or, potentially, far-field RF power transfer. A pair of contact pads enables integration of these and other options in power supply (Fig. 4A and fig. S26). A combined circuit and mechanics iterative design process, similar to that described for the single-channel device, enables a high level of stretchability and low effective modulus. As a consequence, the system can naturally integrate with the skin and remain adhered through van der Waals forces during twisting, stretching, and pinching (Fig. 4B and fig. S27). An EMG

recorded from the forearm during repeated clenching and releasing of the fist is shown in Fig. 4C. The output of the accelerometer during walking and falling appears in Fig. 4D. The temperature responses induced through breathing onto the device (Fig. 4E) and physical exercise are consistent with those observed by using a commercial infrared camera (figs. S28 and S29).

The results presented here establish a general, quantitative experimental and theoretical framework for hard/soft composite systems that exploit (i) microfluidic suspensions to mechanically isolate rigid materials from compliant, elastomeric enclosures, (ii) topographical features and patterned surface chemistries to control interface adhesion, and (iii) self-similar structural designs to provide hierarchical buckling mechanics and large elastic strain range. Multifunctional devices that exploit these ideas allow mounting on the skin in ways that are barely perceptible, in a mechanical sense. Additional possibilities include construction of hybrid systems that incorporate epidermal transistors for amplified, multiplexed addressing of signals from distributed arrays of soft sensors, with collections of strain-isolated, chip-scale components for data storage, processing, and RF transmission. Here, replacing the fluids with ultralow-modulus elastomers may capture some of the favorable mechanics and also eliminate the potential for leakage. Areas of potential use range from physiological status monitoring in neo-natal intensive care units to continuous assessment of responses to pharmaceuticals administered in the home, where existing technologies exert undue stresses and levels of discomfort on the patient. These directions—especially when pursued by using recent advances in power-efficient radios (*24*–*26*), wireless energy transfer schemes (*27*–*29*) and functional microfluidics (*14*–*16*)—have potentially broad implications for the future of body-integrated electronics.

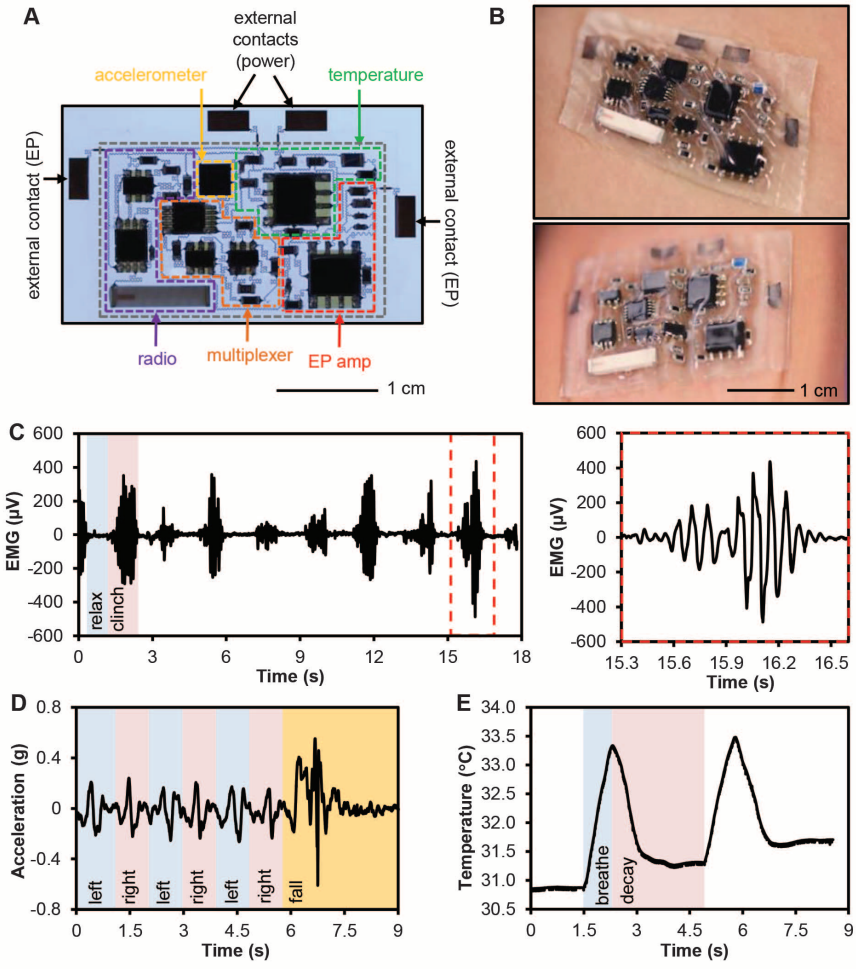

Fig. 4. Images and operational data from a multifunctional wireless sensor. (**A**) Optical image with colored dashed boxes and labels to identify the various subsystems. The gray dashed box around the periphery indicates, approximately, the location of bonding of the superstrate. (**B**) Images of the device on the skin in (top) twisted and stretched and (bottom) compressed states. (**C**) EMG acquired from above the left carpi radialis during periodic clenching and relaxing of the fist. (Right) An enlarged view of the EMG for a single clinching motion. (**D**) Acceleration profiles corresponding to walking, with the device mounted on the forearm. The data near the end of this timeframe corresponds to an intentional fall. (**E**) Temperature response to breathing warm air onto the device. The data shown in this figure were collected by use of a small coin cell battery as a source of power.

References and Notes

1. D. H. Kim *et al.*, *Science* **333**, 838–843 (2011).
2. J.-W. Jeong *et al.*, *Adv. Mater.* **25**, 6839–6846 (2013).
3. M. Kaltenbrunner *et al.*, *Nature* **499**, 458–463 (2013).
4. M. S. White *et al.*, *Nat. Photonics* **7**, 811–816 (2013).
5. M. S. Mannoor *et al.*, *Nat. Commun.* **3**, 763 (2012).
6. J. A. Rogers, M. G. Lagally, R. G. Nuzzo, *Nature* **477**, 45–53 (2011).
7. C. F. Pan *et al.*, *Nat. Photonics* **7**, 752–758 (2013).
8. C. Wang *et al.*, *Nat. Mater.* **12**, 899–904 (2013).
9. S. C. B. Mannsfeld *et al.*, *Nat. Mater.* **9**, 859–864 (2010).
10. D. J. Lipomi *et al.*, *Nat. Nanotechnol.* **6**, 788–792 (2011).
11. T. Sekitani, T. Someya, *MRS Bull.* **37**, 236–245 (2012).
12. G. Schwartz *et al.*, *Nat. Commun.* **4**, 1859 (2013).
13. C. Keplinger *et al.*, *Science* **341**, 984–987 (2013).
14. M. Kubo *et al.*, *Adv. Mater.* **22**, 2749–2752 (2010).
15. E. Palleau, S. Reece, S. C. Desai, M. E. Smith, M. D. Dickey, *Adv. Mater.* **25**, 1589–1592 (2013).
16. D. M. Vogt, Y. L. Park, R. J. Wood, *IEEE Sens. J.* **13**, 4056–4064 (2013).
17. S. Wagner, S. Bauer, *MRS Bull.* **37**, 207–213 (2012).
18. T. Sterken *et al.*, *Conf. Proc. IEEE Eng. Med. Biol. Soc.* **2011**, 6886–6889 (2011).
19. F. Axisa *et al.*, *Conf. Proc. IEEE Eng. Med. Biol. Soc.* **2011**, 5687–5690 (2007).
20. M. Gonzalez *et al.*, *Microelectron. Reliab.* **51**, 1069–1076 (2011).
21. H. Vandeparre, Q. Liu, I. R. Minev, Z. Suo, S. P. Lacour, *Adv. Mater.* **25**, 3117–3121 (2013).
22. A. Romeo, Q. H. Liu, Z. G. Suo, S. P. Lacour, *Appl. Phys. Lett.* **102**, 131904 (2013).
23. S. P. Lacour, S. Wagner, R. J. Narayan, T. Li, Z. G. Suo, *J. Appl. Phys.* **100**, 014913 (2006).
24. Y. Lee, B. Giridhar, Z. Foo, D. Sylvester, D. B. Blaauw, *IEEE J. Solid-State Circuits* **48**, 2511–2521 (2013).
25. Y. Lee *et al.*, *IEEE J. Solid-State Circuits* **48**, 229–243 (2013).
26. Y. Sun, H. Luo, S. K. Das, *IEEE Trans. Depend. Secure Comput.* **9**, 785–797 (2012).
27. E. Y. Chow, M. M. Morris, P. P. Irazoqui, *IEEE Microw. Mag.* **14**, 64–73 (2013).
28. S. Kim, J. S. Ho, A. S. Y. Poon, *Phys. Rev. Lett.* **110**, 203905 (2013).
29. S. J. Thomas, R. R. Harrison, A. Leonardo, M. S. Reynolds, *IEEE Trans. Biomed. Circuit Syst.* **6**, 424–436 (2012).

Acknowledgments: This work was supported by the U.S. Department of Energy, Office of Basic Energy Sciences, Division of Materials Sciences and Engineering under Award DE-FG02-07ER46471 through the Frederick Seitz Materials Research Laboratory at the University of Illinois at Urbana–Champaign, and the Korean Foundation for International Cooperation of Science and Technology (KICOS) through a grant [K2070400000307A050000310, Global Research Laboratory (GRL) Program] provided by the Korean ministry of Science and Technology (MOST). K.E.M was supported by a postdoctoral fellowship from the Beckman Institute. The authors thank V. Malyarchuk, S. H. Ali, Y. Song, T. Banks, and S. Xiang for technical support and stimulating discussions.

Supplementary Materials

www.sciencemag.org/content/344/6179/70/suppl/DC1
Materials and Methods
Figs. S1 to S29
Tables S1 to S3
References (*30*, *31*)
Movies S1 and S2

24 December 2013; accepted 4 March 2014
10.1126/science.1250169

www.sciencemag.org/content/344/6179/70/suppl/DC1

Supplementary Material for

Soft Microfluidic Assemblies of Sensors, Circuits, and Radios for the Skin

Sheng Xu, Yihui Zhang, Lin Jia, Kyle E. Mathewson, Kyung-In Jang, Jeonghyun Kim, Haoran Fu, Xian Huang, Pranav Chava, Renhan Wang, Sanat Bhole, Lizhe Wang, Yoon Joo Na, Yue Guan, Matthew Flavin, Zheshen Han, Yonggang Huang,* John A. Rogers*

*Corresponding author. E-mail: jrogers@illinois.edu (J.A.R.); y-huang@northwestern.edu (Y.H.)

Published 4 April 2014, *Science* **344**, 70 (2014)
DOI: 10.1126/science.1250169

This PDF file includes:

Other Supplementary Material for this manuscript includes the following:
(available at www.sciencemag.org/content/344/6179/70/suppl/DC1)

Movies S1 and S2

Materials and Methods

Design rationale for the circuits

For the inductive electrocardiogram (ECG) system, Chip 105 (10 μF capacitor) is used to block the DC offset of the incoming ECG signal. Chip 107 (0.1 μF capacitor) and chip 13 (200 kΩ) form a high pass resistor-capacitor filter to remove low frequency noise from the incoming ECG signal. The instrumentation amplifier (AD627b, chip 1) amplifies the ECG signal by 800 times. Chip 107 (0.1 μF capacitor) and chip 10(10 kΩ) form a low pass resistor-capacitor filter to remove high frequency noise from the amplified ECG signal collected by the epidermal working and reference electrodes, with a floating ground. A voltage controlled oscillator (MAX2750, chip 3) generates high frequency signals at ~2.4 GHz that represent the ECG signal voltage. The output of this chip passes out of the device through a compact three dimensional antenna (chip 18). A separate patch antenna, radiofrequency (RF) amplifier and frequency counter can receive the transmitted RF wave reliably at a distance of up to 1 m, when operated in a room designed to eliminate background electrical noise. The inductive power module is based on resonant inductive coupling: a 10 μH inductive coil (27T103C, chip 101) and 0.1uF capacitor (chip 107) forms an inductor-capacitor loop. A Schottky diode provides rectification and a capacitor (10 μF) provides integration.

For the multifunctional device, the electrophysiological (EP) amplification subunit is similar to that of the ECG system. The acceleration sensing module consists of chip 6 (KXTH9) which converts acceleration to an analog voltage output. The temperature sensing module uses a Wheatstone bridge circuit to convert temperature to an analog voltage output. Chip 5 (PTS080501B500RP100) is a resistance temperature detector. Chips 16 and 17 are paired resistors to form the bridge loop. In the multiplexing module, chip 21 (LTC6991) generates an oscillating signal that controls the multiplexer (MAX4734, chip 2), to switch sequentially among the outputs of the three sensor channels, EP, temperature and acceleration sensing, to allow data transmission with a single voltage controlled oscillator. In particular, data from the EP, acceleration and temperature channels transmit for 18, 9 and 9 seconds, respectively, as determined by two oscillators that generate two bit control logic by tuning the ratio of their oscillation frequencies to 1:2. A pulse width modulation oscillator periodically turns on and off the voltage controlled oscillator, for a duty cycle of ~7% at a frequency of 1000 Hz, to reduce the average power consumption from ~40 mW (continuous operating mode) to ~6.3 mW. The wireless data transmission subunit is similar to that of the ECG system.

Molding structures of surface relief on the elastomeric device substrate

The process began with a piece of a clean (100) Si wafer, coated with a 100 nm thick Si_3N_4 film formed by plasma enhanced chemical vapor deposition (STS PECVD). Photolithography (AZ P4620, 3000 rpm, 30 s, soft bake at 110 °C for 3 min, 300 mJ/cm^2, 1:2 volume ratio of AZ 400K and de-ionized water for 1 min) and reactive ion etching (RIE, 22.5 sccm CF_4, 40 mT, 150 W, 8 min) defined an array of circles (20 μm∅) in the Si_3N_4. Wet chemical anisotropic etching of the silicon with KOH (100 ml 33% weight percent water solution, 20 ml isopropanol alcohol, 130 °C, 45 min, with strong magnetic stirring) generated an array of pyramidal shaped recessed regions on the surface of the wafer. After removing the remaining Si_3N_4, a second photolithography step (AZ P4620)

and inductively coupled plasma reactive ion etching process (ICP RIE, Bosch process) defined trenches (30 μm in depth) for the support posts for the chips. A third photolithography step (AZ P4620) and RIE process (STS ICP RIE, Bosch process) defined the trenches (100 μm in depth) for the isolation barriers. A layer of polytetrafluoroethylene (~200 nm) conformally deposited (STS ICP RIE) all exposed surfaces to minimize adhesion. Thin (300 μm) silicone substrates (Ecoflex, Smooth-On) were prepared by mixing the two components of a commercial kit in a 1:1 weight ratio, spin-casting (300 rpm for 30 s) the resulting material onto the processed Si wafer and then curing into a solid form (2 hours at room temperature).

Fabrication of the interconnect network

The process began with spin casting of polydimethylsiloxane (PDMS, Sylgard 184), mixed at 10:1 ratio, onto a clean glass slide at 3000 rpm for 30 s. After curing in an oven at 70 °C for 2 hours, the PDMS was exposed to oxygen plasma (20 sccm O_2, 300 mT, 200 W, 30 s). A 2.4 μm thick layer of polyimide (PI, from poly(pyromellitic dianhydride-*co*-4,4′-oxydianiline) amic acid solution was then applied by spin casting (2000 rpm for 60 s), baked on a hotplate at 150 °C for 4 mins and in a vacuum oven at 10 mT and 250 °C for 1 h. The interconnects and metal electrodes consisted of a 400 nm thick layer of Cu deposited by electron beam evaporation onto the PI. Photolithography (AZ P4620) and etching (CE-100 copper etchant, Transene Company) defined patterns in the Cu. Next, spin coating formed a second 2.4 μm thick layer of PI over the entire structure. A 50 nm thick layer of SiO_2 was then deposited using electron beam evaporation, to serve as an etching mask for the PI. Next, photolithography (AZ P4620), RIE etching (50 mT, 40 sccm CF_4, 100 W, 20 min), and oxygen plasma etching (20 sccm O_2, 300 mT, 200 W for 21 mins) patterned the layers of PI in a geometry matched to the metal traces. The residue SiO_2 mask was removed using buffered oxide etchant, and the overall circuit electrodes were immersed in electroless Sn plating solution (Transene Company) at 80 °C for ~10 s. The Sn deposited only onto the exposed Cu surfaces, for the purpose of ensuring good wettability of the solder on the bonding pads. Finally, the circuit electrodes were retrieved using water soluble tape (3M, Inc.) for aligned transfer to the device substrate.

Assembly of the chip components

Electron beam evaporation of Ti (5 nm) / SiO_2 (50 nm) on the pads (mounting sites for the chips) of the interconnect network formed backside coatings *(30)*. A shadow mask made of PI (Stencilunlimited corp.) with patterns matched to the support posts, was aligned and laminated onto the molded silicone substrate (thickness ~0.4 mm). The substrate was then activated by exposure to ultraviolet induced ozone for 5 mins. Aligning and laminating the interconnect network onto this surface led to an irreversible strong bonding upon contact, only at the locations of the support posts (~1 mm diameter). After aging for 10 mins, the water soluble tape was removed by immersion in tap water for 1 hour. Another shadow mask, the same as the one for electroless Sn plating, was then aligned and laminated onto the electrodes to selectively expose the contact pads for the pin contacts associated with each of the component chips. A $Sn_{42}Bi_{58}$ alloy solder paste (Chip Quik Inc. SMDLTFP250T3) was screen printed onto the contact pads. A combined lapping and polishing process with tripod polisher was used for thinning of the thickest

chips, such that all chips had thicknesses <1 mm. The lapping process involved a fast back grinding step, followed by a polishing process to remove remaining rough surfaces. Each chip component was manually placed over the electrodes under an optical microscope. After all of the chips were in position, the solder paste was reflowed in an oven at ~180 °C for 5 mins. Good solder joints appeared smooth and shiny, with complete wetting to the contact pads. A thin silicone superstrate (~100 μm thick) encapsulated the entire chip region of the device. The edges were sealed with an additional application of partially cured silicone followed by baking on a hotplate at 120 °C for 10 min. A liquid PDMS base (Sylgard 184, without the curing agent), injected into the capped cavity through an edge, covered all of the chips and interconnects via capillary force.

Mechanical testing and simulation of the devices

An array of metal dots (100 nm Cr, 0.4 mm∅ for each dot, 1 mm pitch) was deposited through a polyimide shadow mask mounted on the back side of the relief substrate. After integrating the interconnect network and chips and adding a thin layer of PDMS base, equal-biaxial stretching was applied to the device using a customized stage. Strain was added/removed gradually and simultaneously in both directions. Images of the device at various stages of deformation were collected with a digital single-lens reflex camera from the backside the device so that the metal dots were clearly visible. The Young's moduli of the devices with and without the chips and interconnect network were measured in orthogonal directions using an INSTRON MINI44. The strain-stress curves were averaged over at least three individual measurements. Mechanical simulation was performed using finite element analysis (FEA) techniques.

Full three-dimensional (3D) FEA was adopted to analyze the postbuckling behaviors of the entire device under uniaxial and biaxial stretching. The chips were selectively bonded to the silicone substrate (Ecoflex; thickness 0.5 mm) via small circular (diameter 1 mm) and rectangular (0.5 mm by 1.0 mm) pedestals. Each of the metal interconnect (Cu, thickness 400 nm) lines, was encased, top and bottom, by a thin layer of polyimide (PI, thickness 2.4 μm for each layer). The elastic modulus (E) and Poisson's ratio (v) are $E_{Ecoflex}$=0.0623 MPa and $v_{Ecoflex}$=0.49 for Ecoflex; E_{Cu}=119 GPa and v_{Cu}=0.34 for copper; and E_{PI}=2.5 GPa and v_{PI}=0.34 for PI. Eight-node 3D solid elements and four-node shell elements were used for the ecoflex and self-similar electrode, respectively, and refined meshes were adopted to ensure the accuracy. Linear buckling analyses were carried out to determine the critical buckling strain and lowest buckling mode for each interconnect, which were then implemented as initial geometric imperfections in the postbuckling simulation. The evolution of deformed configurations with applied strains were obtained from FEA for the entire device under both uniaxial and biaxial stretchings, as shown in Figs. 2, S11, S13, and S14. Good agreement between FEA and experiment results can be found.

Functional testing of the devices on human subjects

All experiments on human were conducted under approval from Institutional Review Board at the University of Illinois at Urbana-Champaign (protocol number: 13398). There are three subjects (age: 21–29, all males), co-authors in the paper. Research was carried out with informed signed consents from the subjects. Prior to

device integration, hairs were removed and the skin was cleaned using a mild abrasive and Scotch tape to exfoliate some of the stratum corneum and to remove sebaceous oils *(31)*. Afterwards, the device was placed on the desired areas on the skin for recording of EP signals. For near field coupling powering, a high frequency alternating current source (10 V_{p-p} at 150 kHz) to the primary coil was generated using a KEITHLEY 3390 50 MHz arbitrary waveform generator. The input and output characteristics of the wireless coil were measured using an Agilent infiniium DSO8104A oscilloscope (1 GHz, 4 channels). The ECG data were received by a back end antenna, then filtered through a 2.2-2.7 GHz band pass filter (RF-lambda, RBPF2450, SN: 12041902227), amplified by a 2.2-2.7 GHz low noise amplifier (ZQL-2700MLNW+), and read out by a frequency counter, where the frequency-modulated signals were processed and analyzed. For recordings with commercial equipment, we used a pair of Au/Ag ring electrodes, fixed with an adhesive sticker to the skin along with conductive electrode gel. A ground electrode was attached on a more proximal section of the right arm. The wireless system, placed directly adjacent to the electrodes used for measurement with the commercial system (Brain Vision V-Amp, with a nearby ground electrode on a distal position on the left forearm), utilized a floating ground. Recorded data were passed through band pass filters to remove line noise and other high frequency artifacts, as well as slow drifts in the signal. The mean voltage of each signal was subtracted to remove the DC offsets. The data were then normalized to their peak values, to facilitate comparisons.

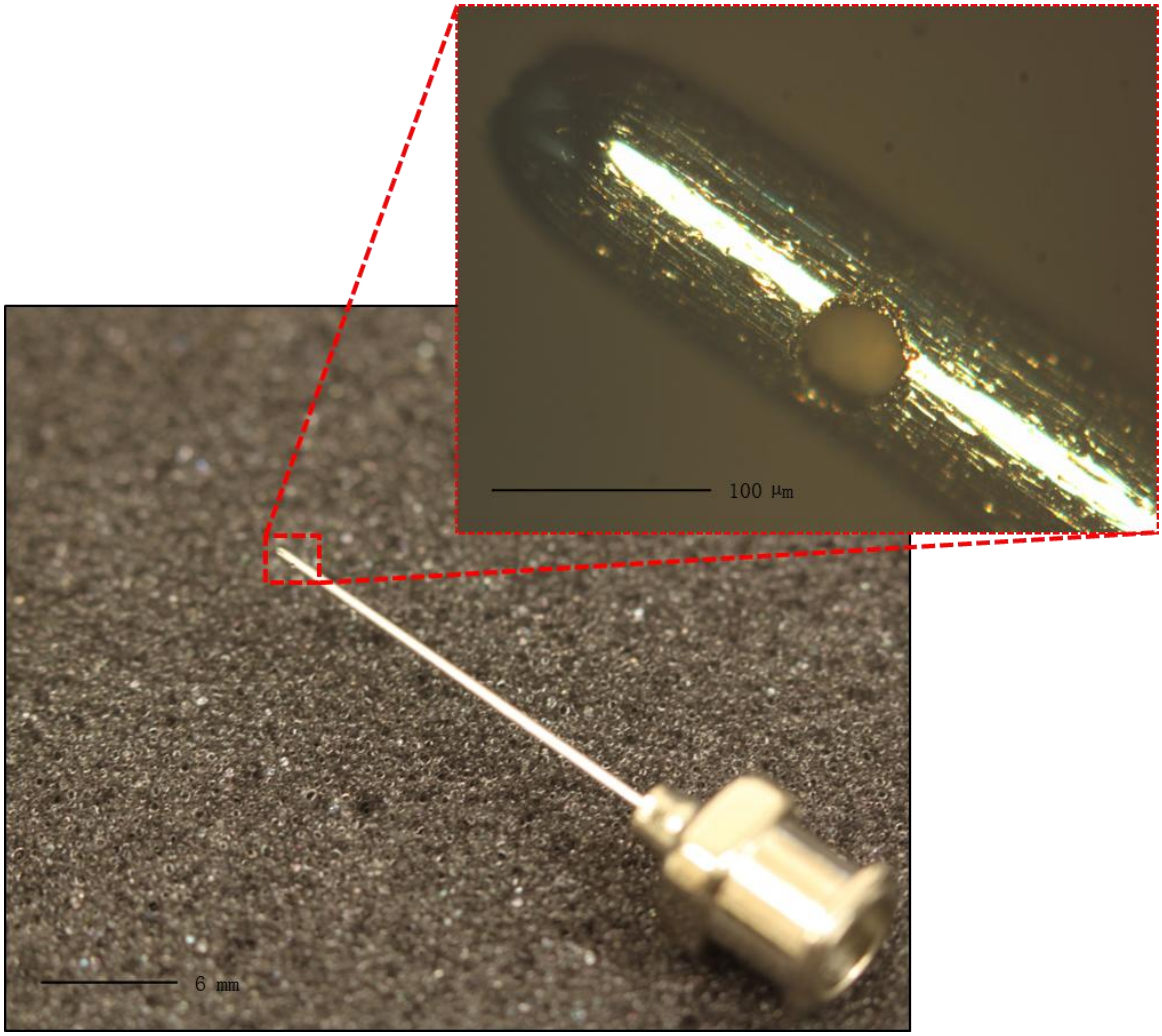

Fig. S1.

Optical image of the non-coring needle, highlighting the inject pore on the side wall of the needle. This construction avoids removal of subject material during the injection process. The elastomer self-seals after removal of the needle. Additional elastomer can be added to enhance the robustness of this seal.

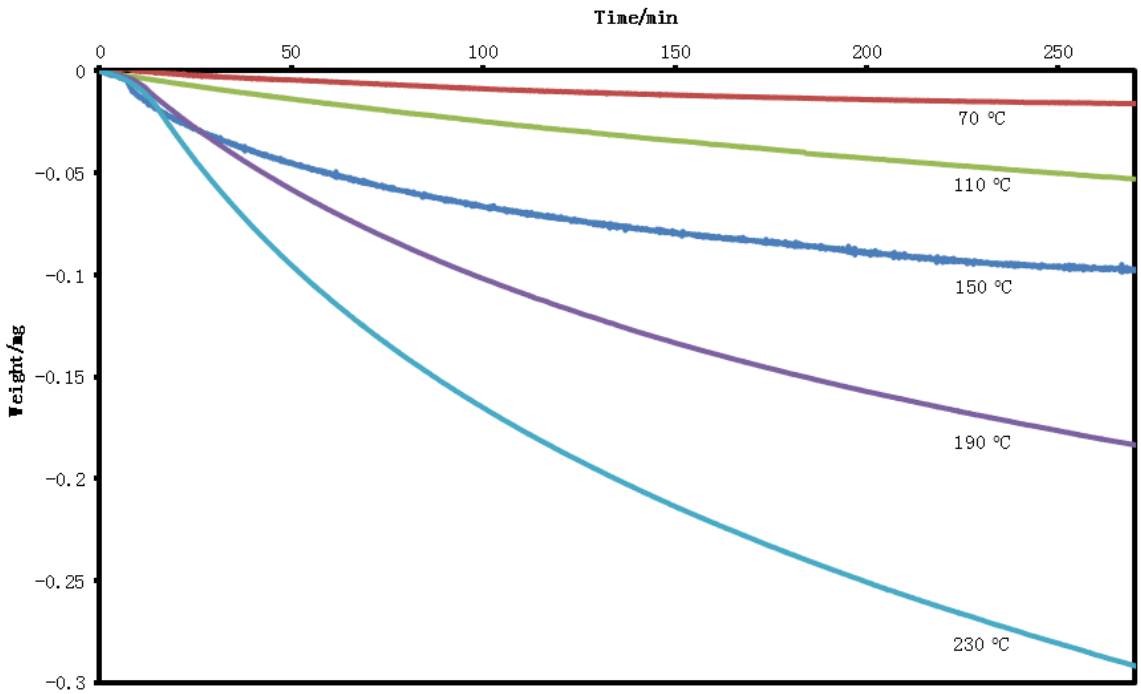

Fig. S2

Thermogravimetric analysis of 10.12 mg PDMS base fluid at elevated temperatures for prolonged time.

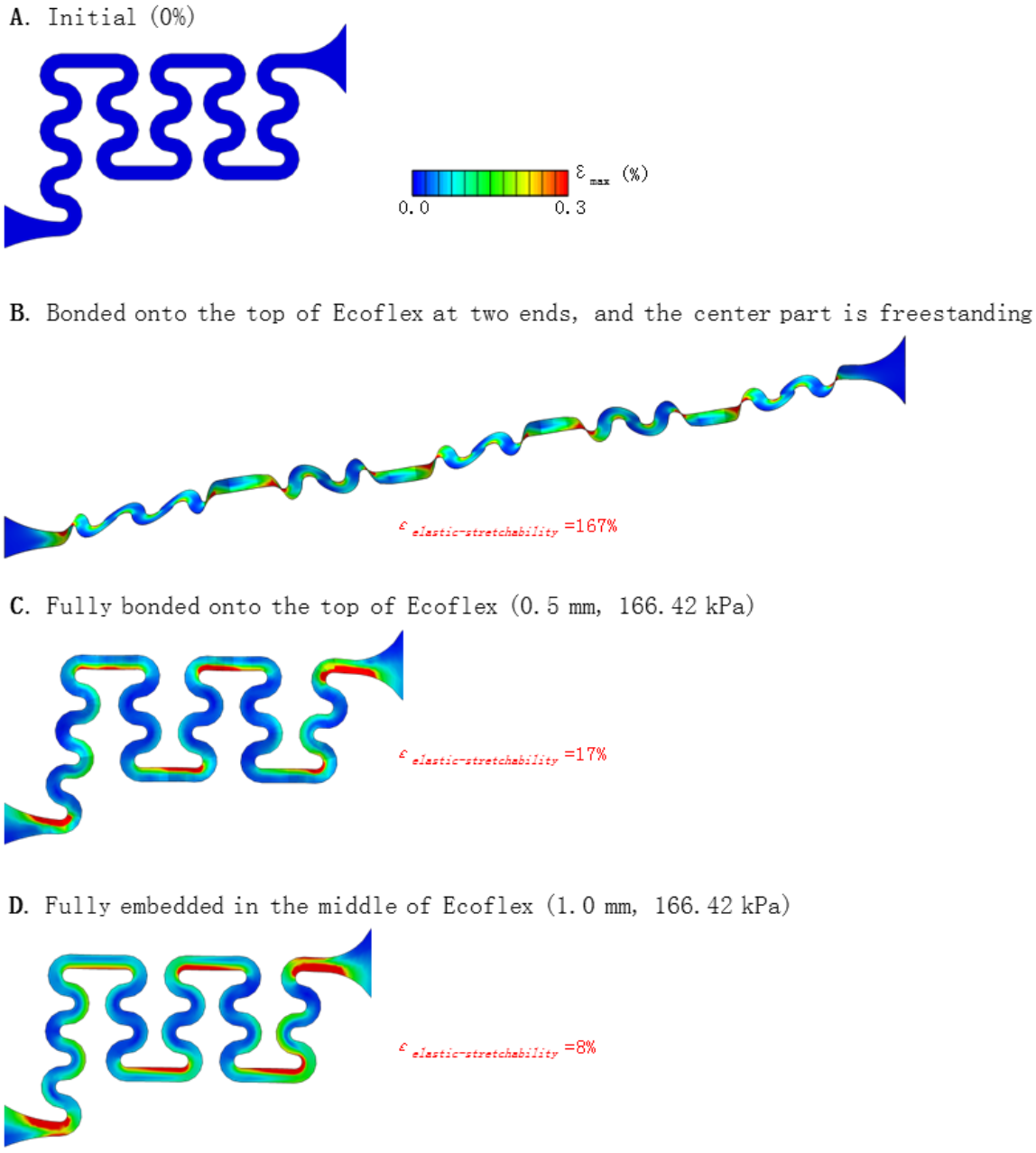

Fig. S3

3D-FEA results that illustrate the mechanics advantage of free-floating interconnects in comparison with fully bonded or embedded ones. (**A**) Initial configuration of one of the interconnects shown in **Fig. 1C**; (**B**) the strain distribution of the interconnect only with two ends bonded onto the top of the Ecoflex, when the applied strain reaches the corresponding elastic stretchability (167%) of the interconnect; (**C**) the strain distribution of the interconnect fully bonded onto the top of the Ecoflex, when the applied strain reaches its elastic stretchability (17%); (**D**) the strain distribution of the interconnect fully embedded in the middle of the Ecoflex, when the applied strain reaches its elastic stretchability (8%).

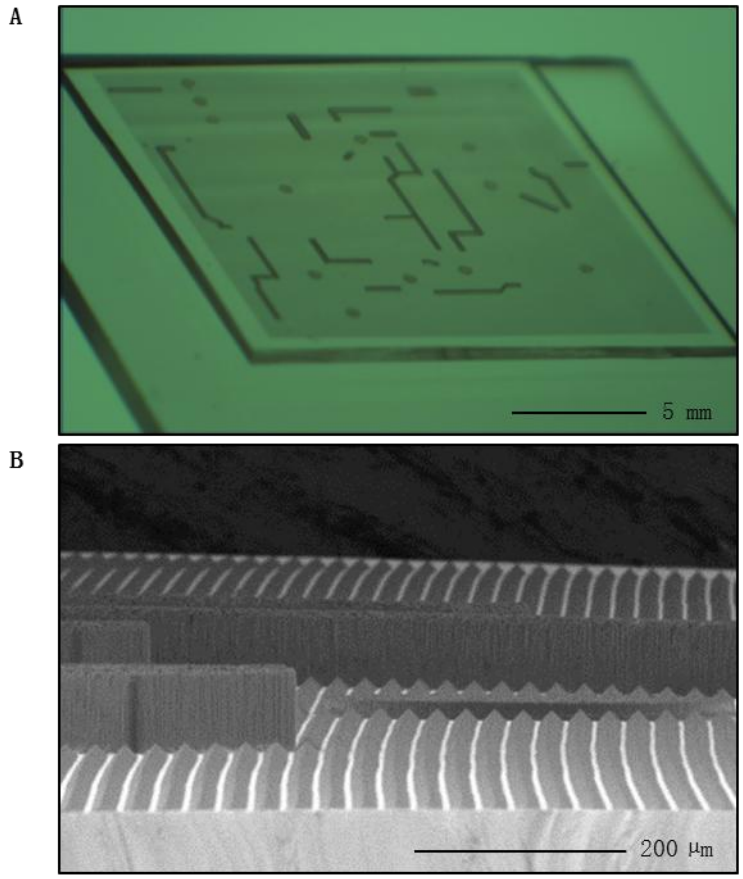

Fig. S4

Characterization of the hierarchical substrate. (**A**) Optical image of a substrate with multiple levels of embossed relief. (**B**) SEM image of a small region of the substrate to illustrate its hierarchical structure.

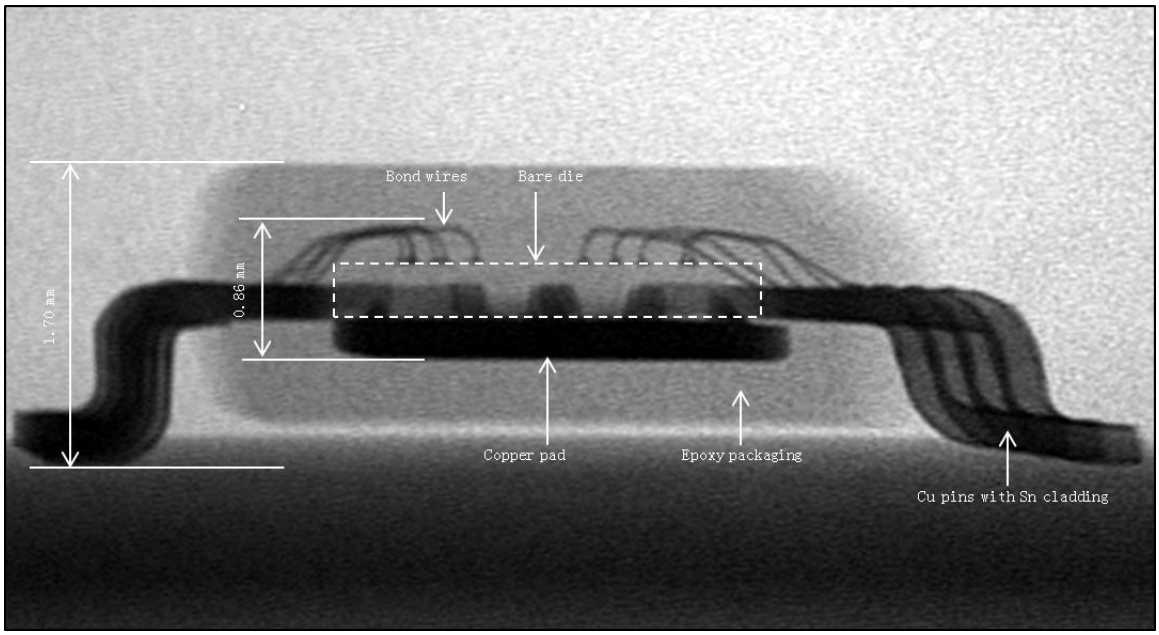

Fig. S5

X-ray side view image of a typical commercial chip with standard package design. The thickness of this chip can be reduced to 0.86 mm by grinding the excessive packaging epoxy away.

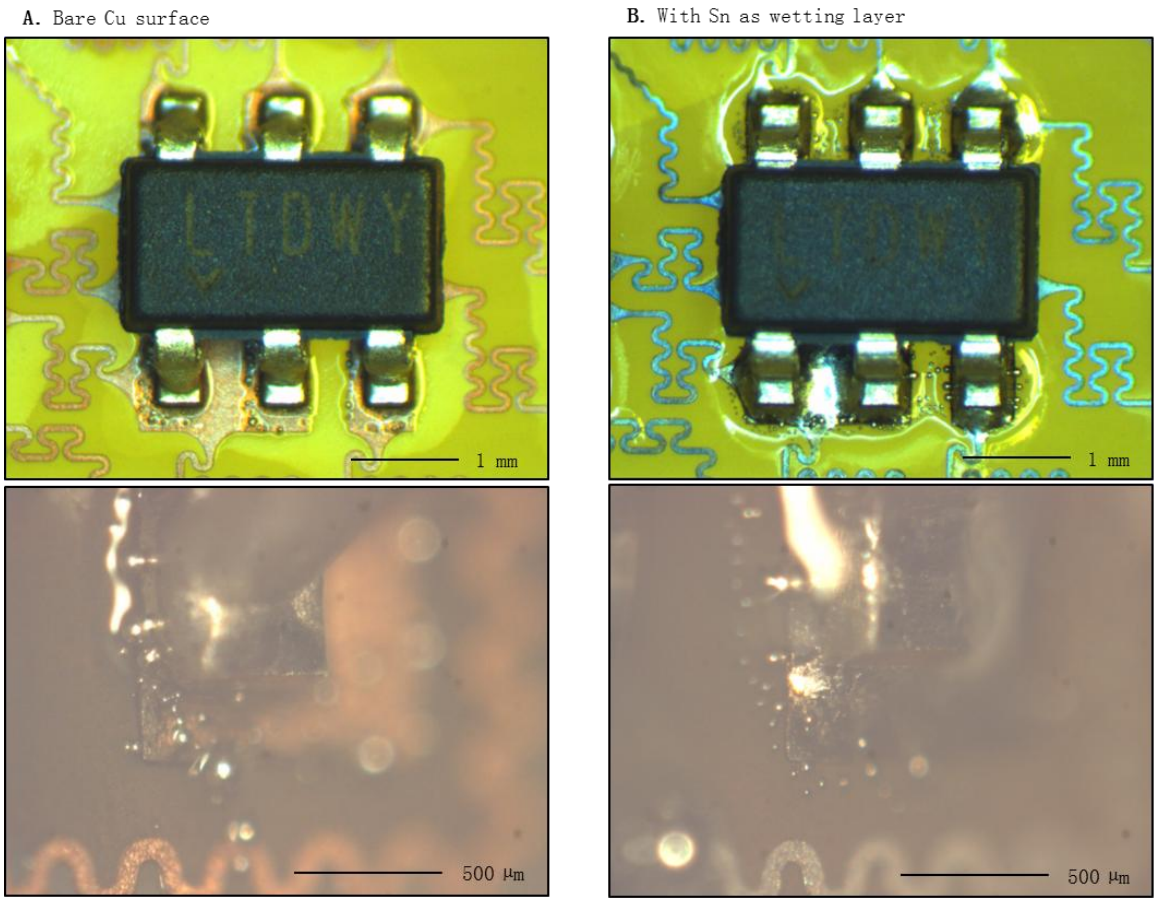

Fig. S6

Optical images of the interface wetting behavior of the interconnects. Chips bonded on the interconnects (**A**) before and (**B**) after electroless Sn plating. These images clearly show that after Sn plating, the $Sn_{42}Bi_{58}$ solder paste, applied by screen printing, can wet the interconnector surfaces well and thus allow a robust bonding interface.

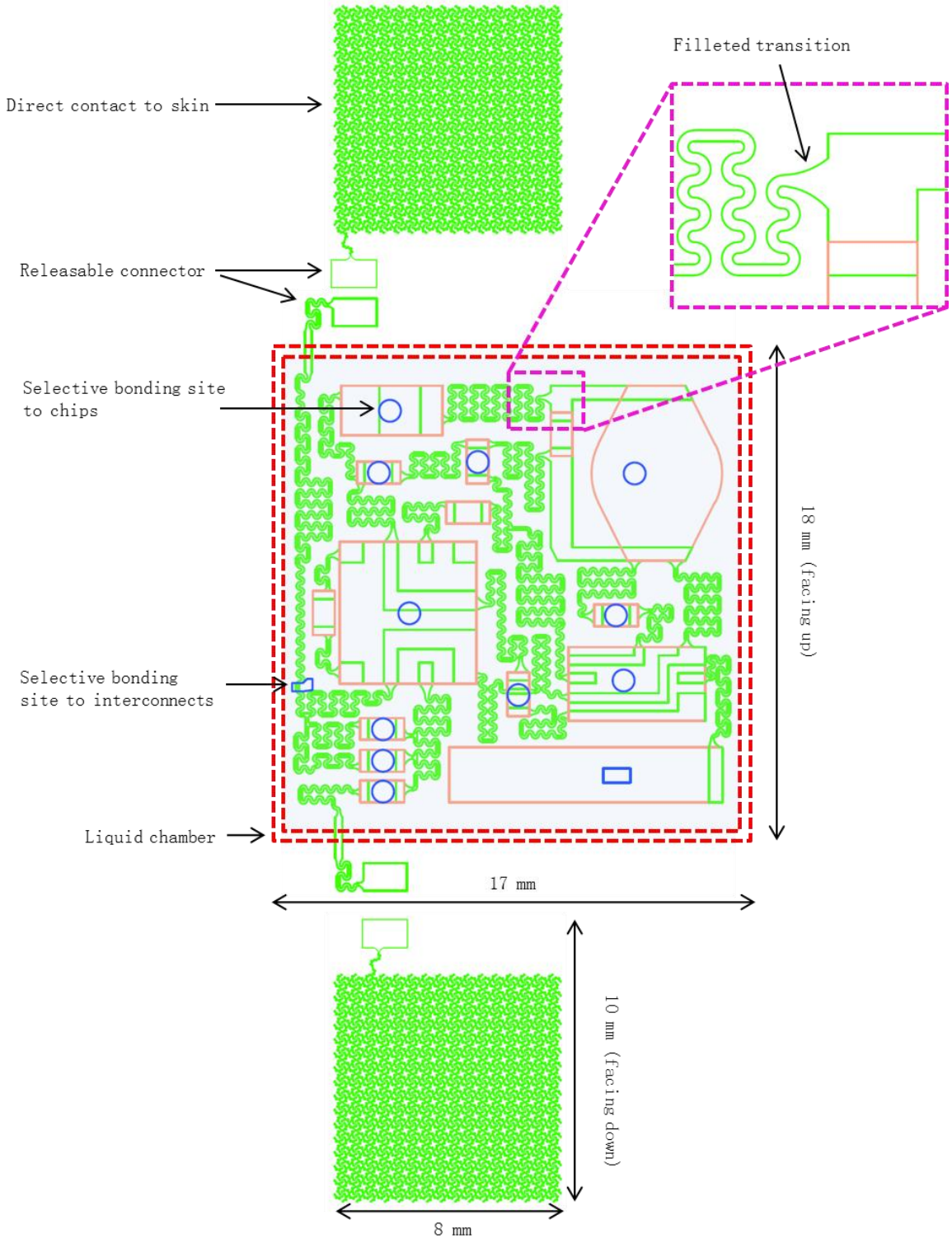

Fig. S7

Layout design of the single ECG system, with labels for different parts of the device. The design of the transition region between the interconnectors and the chip bonding pads, to minimize stress concentration, is also highlighted in the dashed purple box.

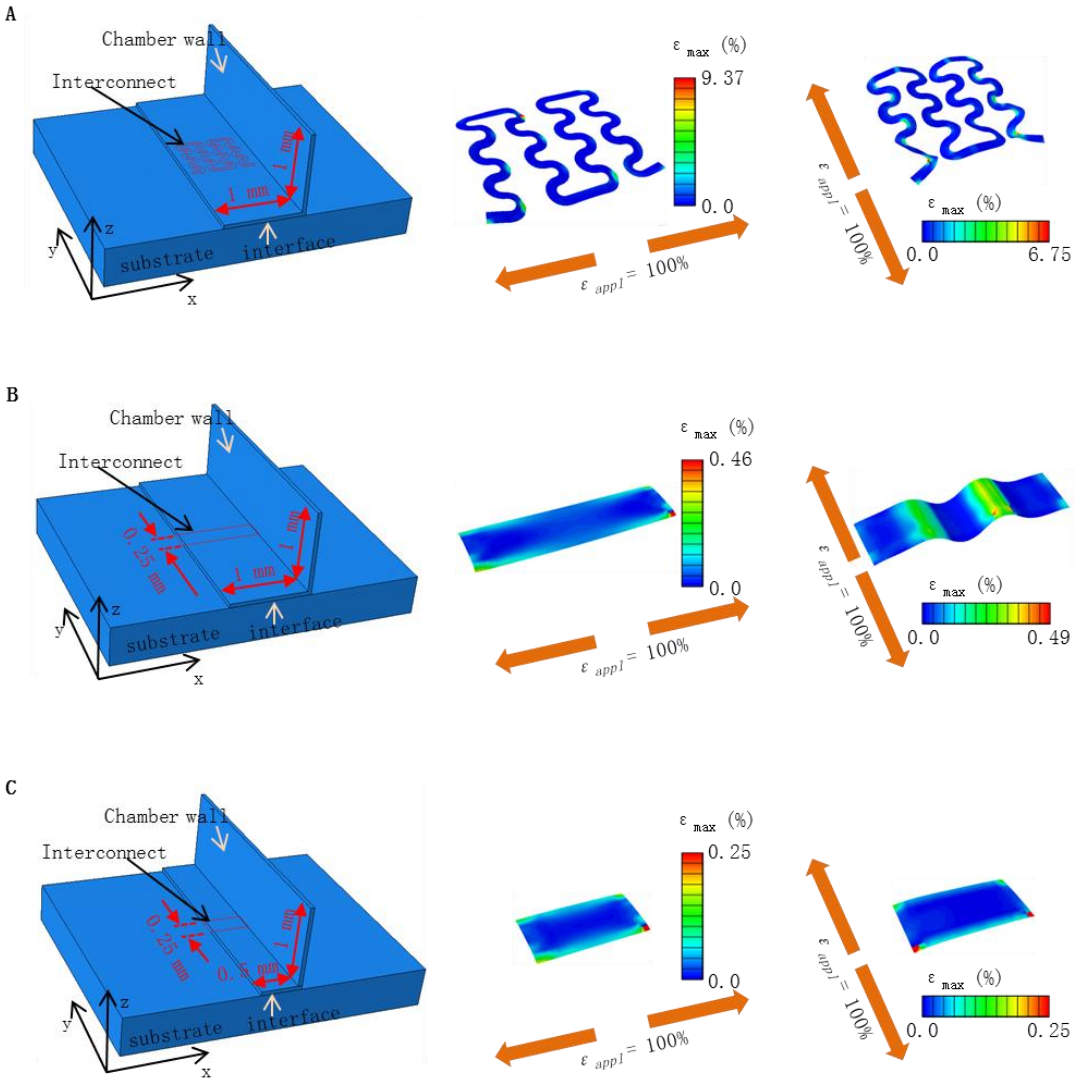

Fig. S8

Comparison of mechanical performance of three different interconnect designs at the point of the periphery of the microfluidic enclosure. (**A**) Schematic illustration (left panel) of a self-similar serpentine interconnect across the interface, and the distribution of maximum principal strain (middle panel for horizontal stretching along the *x* direction; right panel for vertical stretching along the *y* direction) in the metal layer for 100% uniaxial stretching. (**B**) Schematic illustration (left panel) of a straight interconnect (length 1 mm) across the interface, and the distribution of maximum principal strain (middle panel for horizontal stretching; right panel for vertical stretching) in the metal layer for 100% uniaxial stretching. (**C**) Schematic illustration (left panel) of a straight interconnect (length 0.5 mm) across the interface, and the distribution of maximum principal strain (middle panel for horizontal stretching; right panel for vertical stretching) in the metal layer for 100% uniaxial stretching. The simulation shows that the optimized straight interconnect at the interface avoids fracture inducing strains even under 100% biaxial stretching, in agreement with the FEA results, where the strain of interconnect remains well below the fracture limit (~5%).

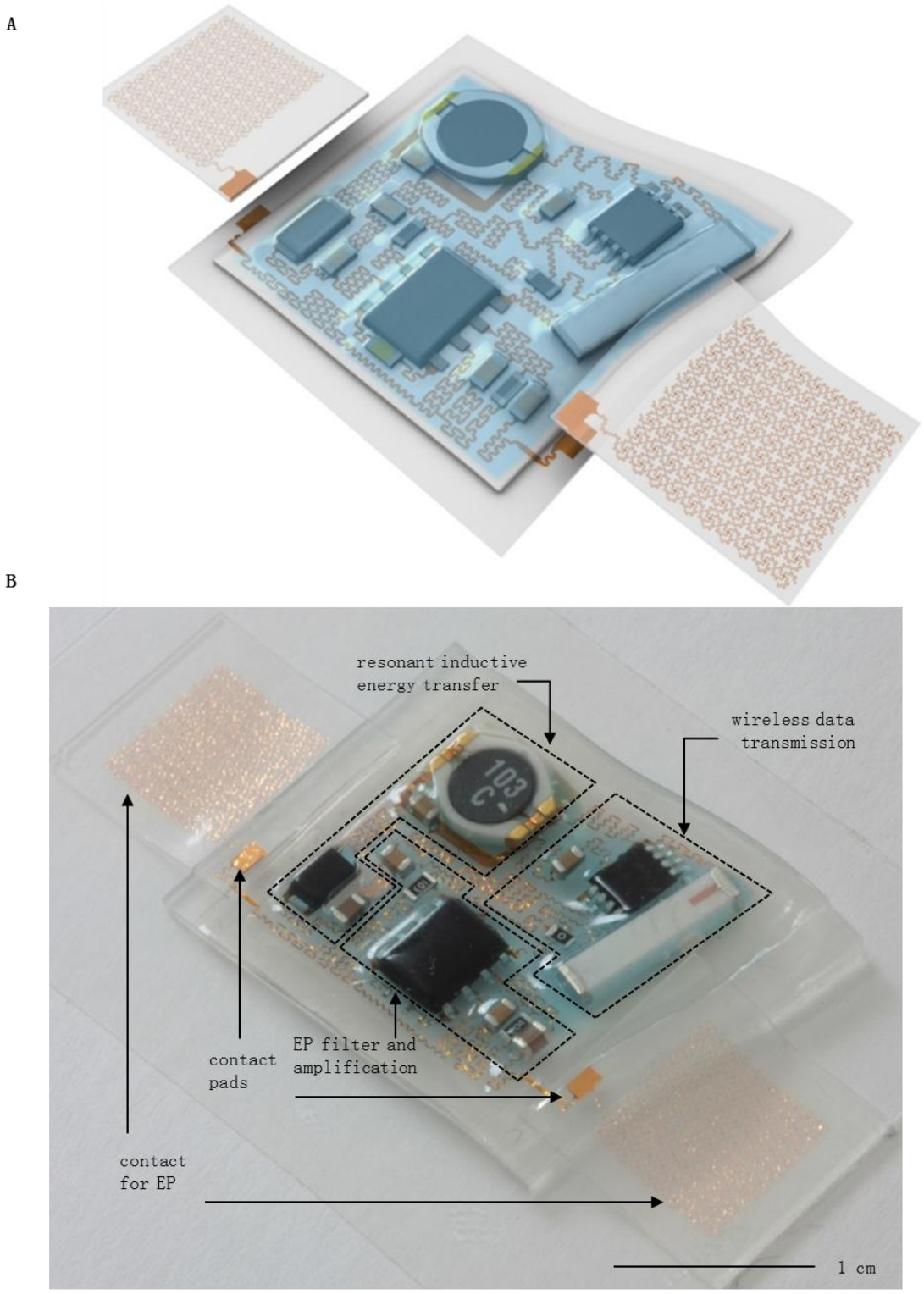

Fig. S9

Illustration of the fully integrated device. (**A**) Schematic illustration of a device in a slightly deformed configuration, and (**B**) optical image of an actual device in a similar state of deformation, with labels for different parts and modules in the circuit.

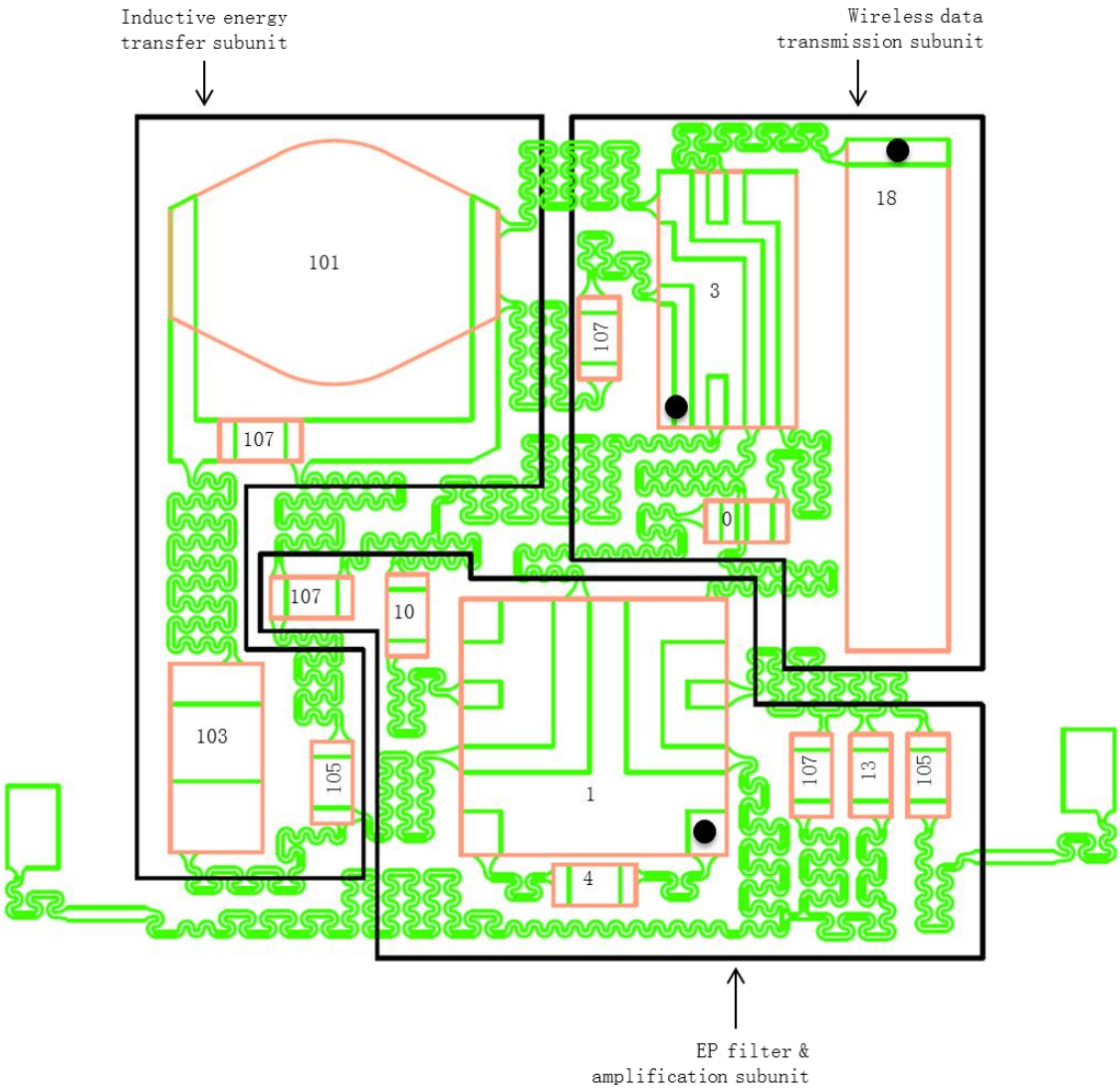

Fig. S10

Schematic layout of the ECG system with the chip positions and chip types (Table S1) labeled. Black dots indicate the number 1 pin of each individual chip.

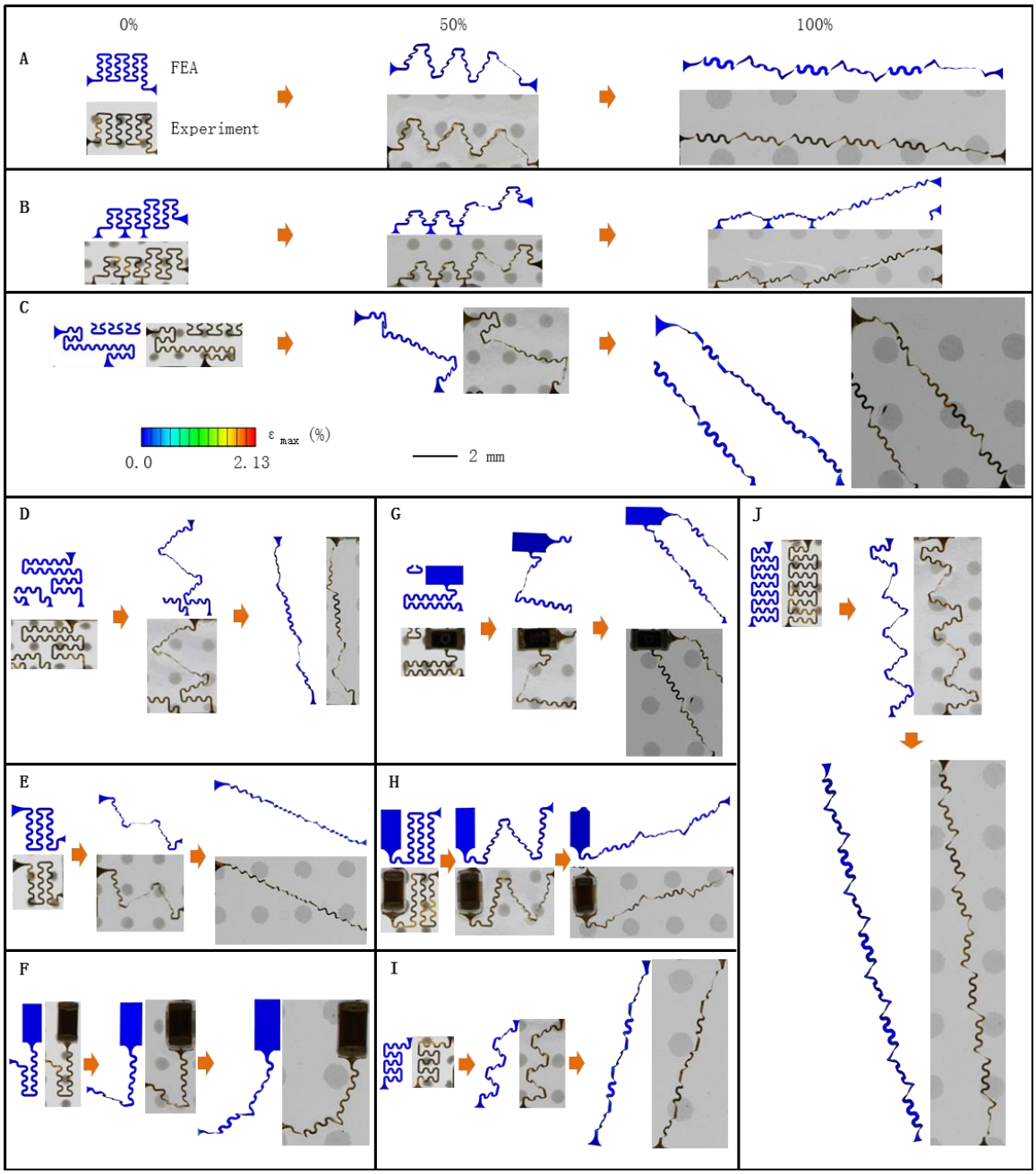

Fig. S11

Experimental and computational studies of localized deformations in various self-similar serpentine interconnects within the ECG system, under biaxial stretching. (**A**) to (**J**) show optical images and corresponding FEA results for ten self-similar serpentine interconnects as the entire circuit is biaxially stretched from 0% to 50% and 100%. The color in the FEA results represents the maximum principal strains of the metal layer.

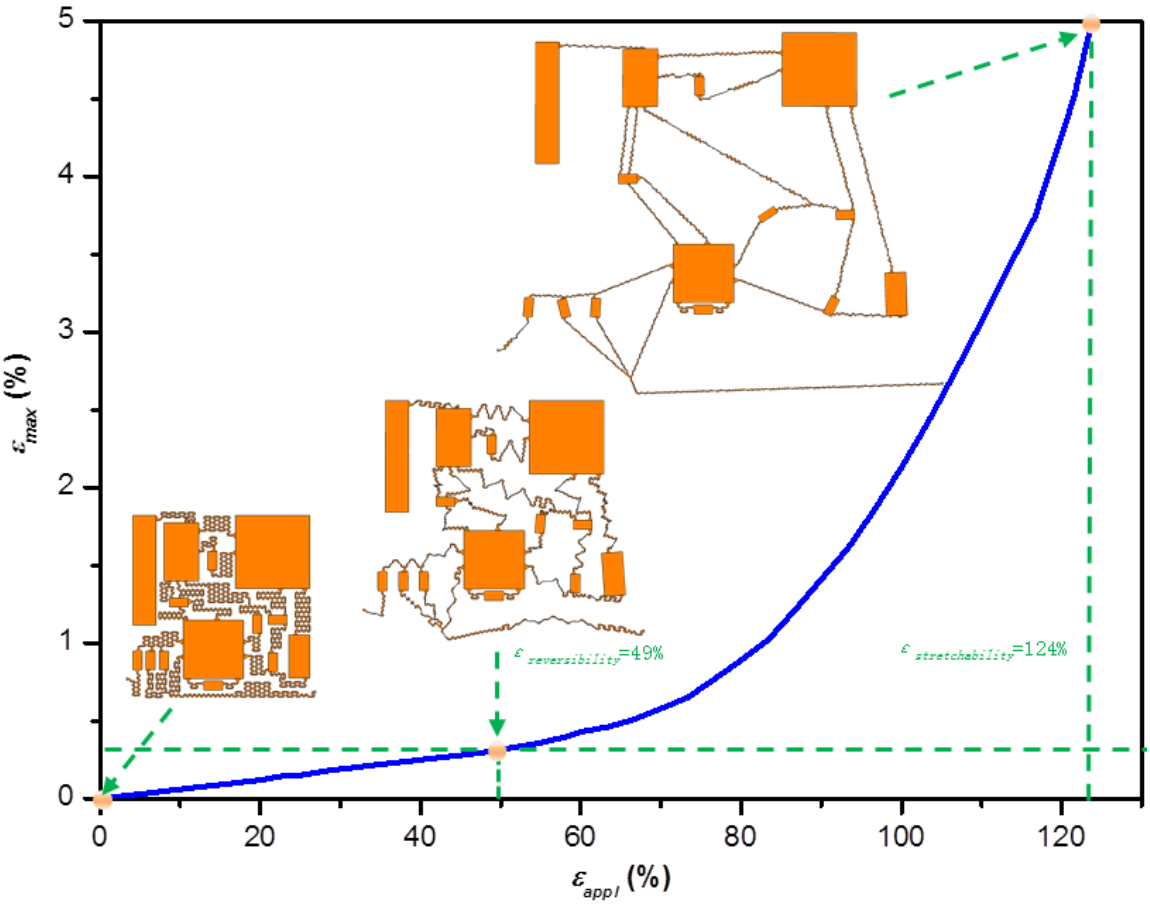

Fig. S12

Dependence of the strain in the interconnect metal (at the material level) on the applied strain (at the system level). The maximum value (ε_{max}) of the principal strain in the metal layer of the interconnect network as a function of the biaxial applied strain (ε_{appl}), together with illustrations of the evolution of the deformations.

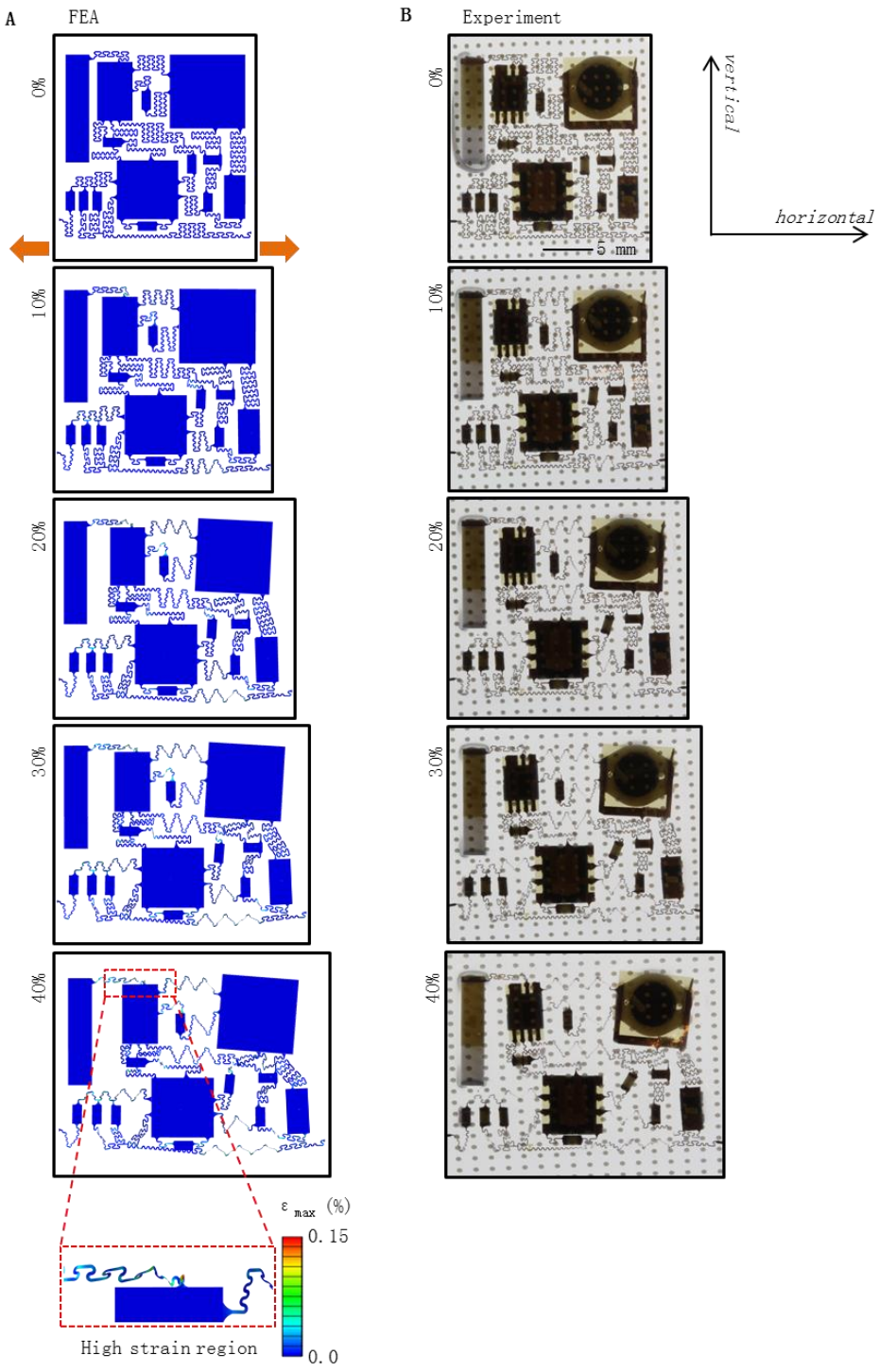

Fig. S13

Experimental and computational studies of buckling deformations across the entire circuits under uniaxial stretching along the horizontal direction. 3D-FEA results (**A**) and corresponding optical images (**B**) of the entire circuit when uniaxially stretched from 0% to 10%, 20%, 30% and 40%. The color in the FEA results represents the maximum principal strains in the metal layer.

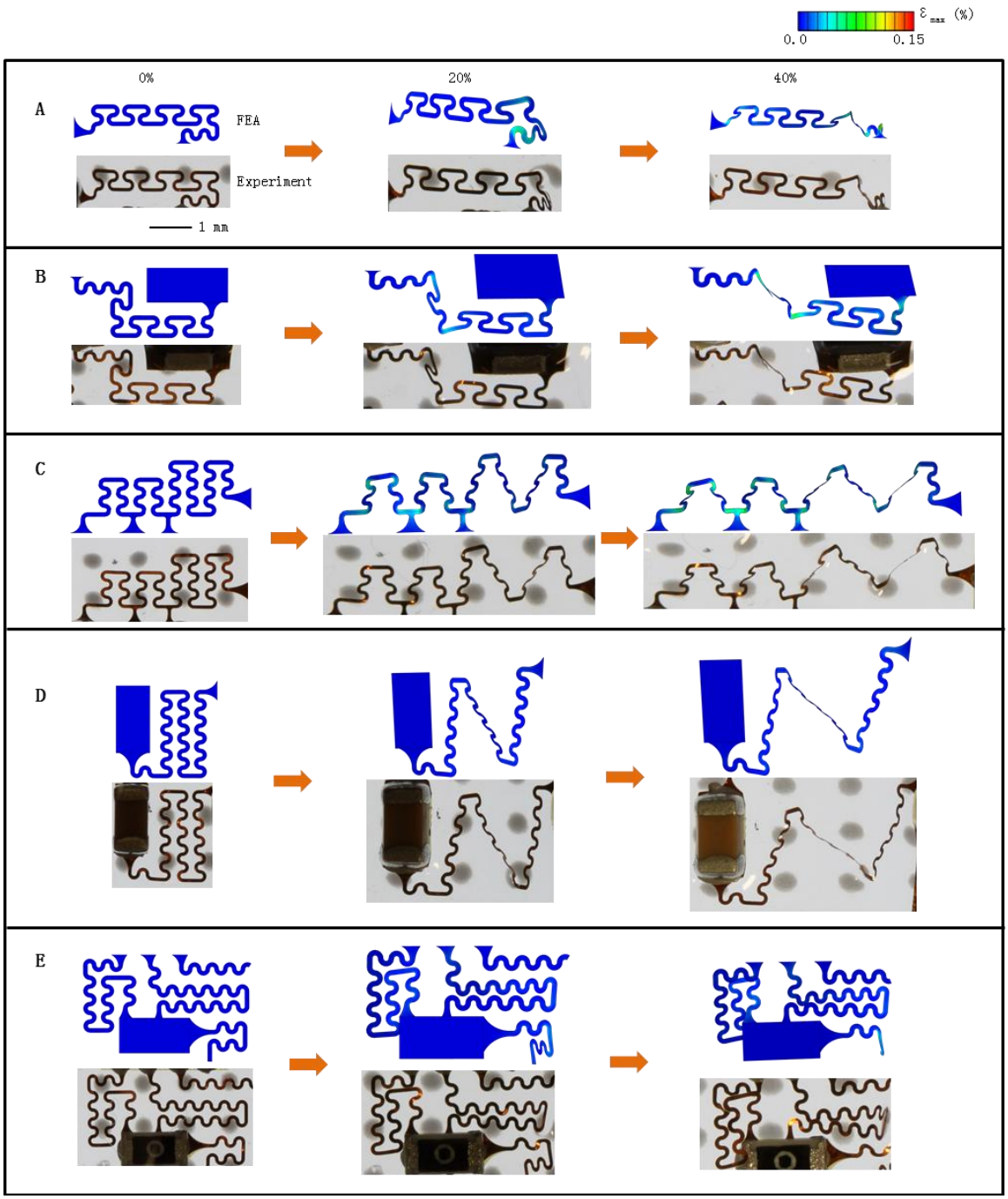

Fig. S14

Experimental and computational studies of localized deformations of self-similar serpentine interconnects with the circuits under uniaxial stretching along the horizontal direction. (**A**) to (**E**) show optical images and corresponding 3D-FEA results of five self-similar serpentine interconnects as the entire circuit is uniaxially stretched from 0% to 20% and 40%. The color in the FEA results represents the maximum principal strains of the metal layer.

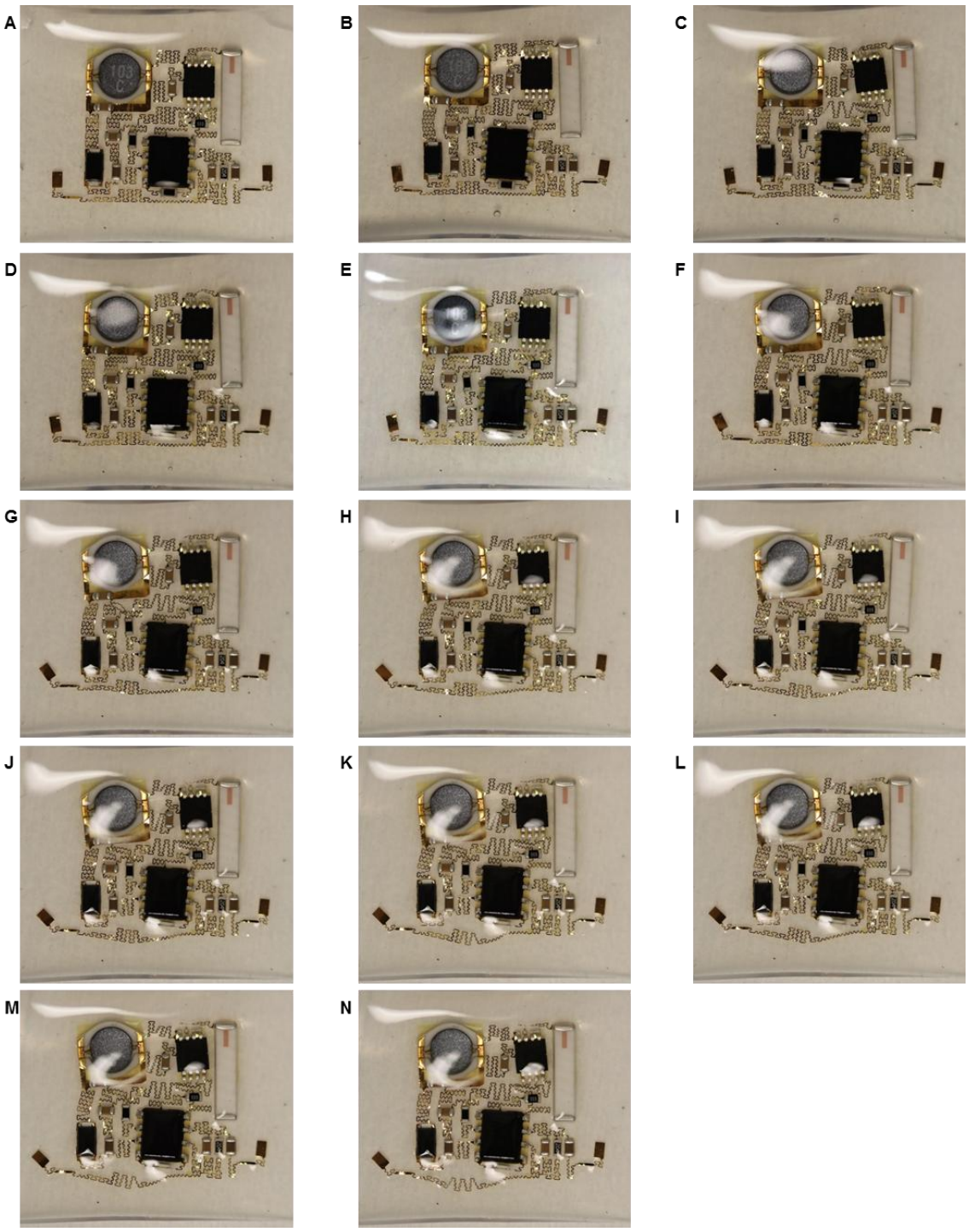

Fig. S15

Cycling testing the ECG device under uniaxial strain with amplitude of 30% at a frequency of 0.6 Hz. (**A**-**N**) Images of the device at 500 cycle increments, up to 6500 cycles.

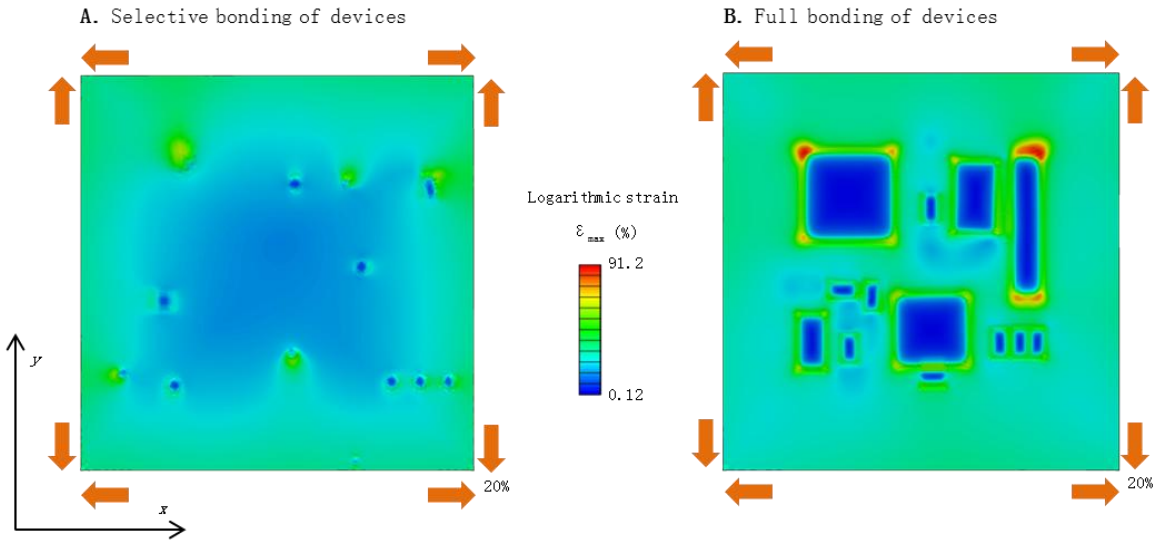

Fig. S16

Finite element simulations to illustrate the effects of rigid devices on the strain distribution across the soft substrate under biaxial stretching of ε_{appl}=20%. (**A**) The distribution of logarithmic strain in the substrate when the rigid devices are selectively bonded to the substrate (via small circular and rectangular pedestals). (**B**) The distribution of logarithmic strain in the substrate when the full regions of each device are bonded to the substrate.

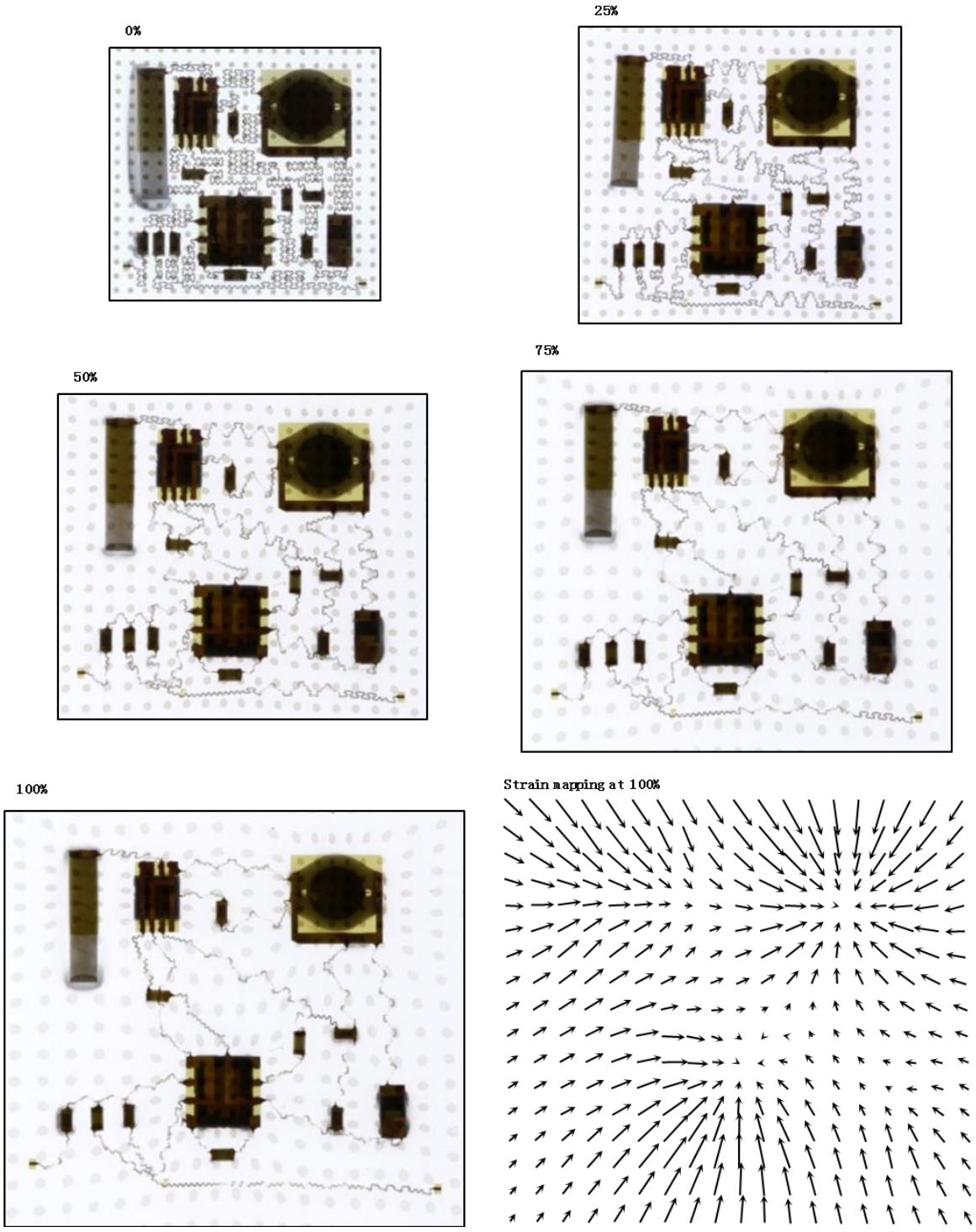

Fig. S17

Strain mapping at different levels of strain when all of the chips are fully bonded on the substrate. The strain localization can be clearly visualized under these chips.

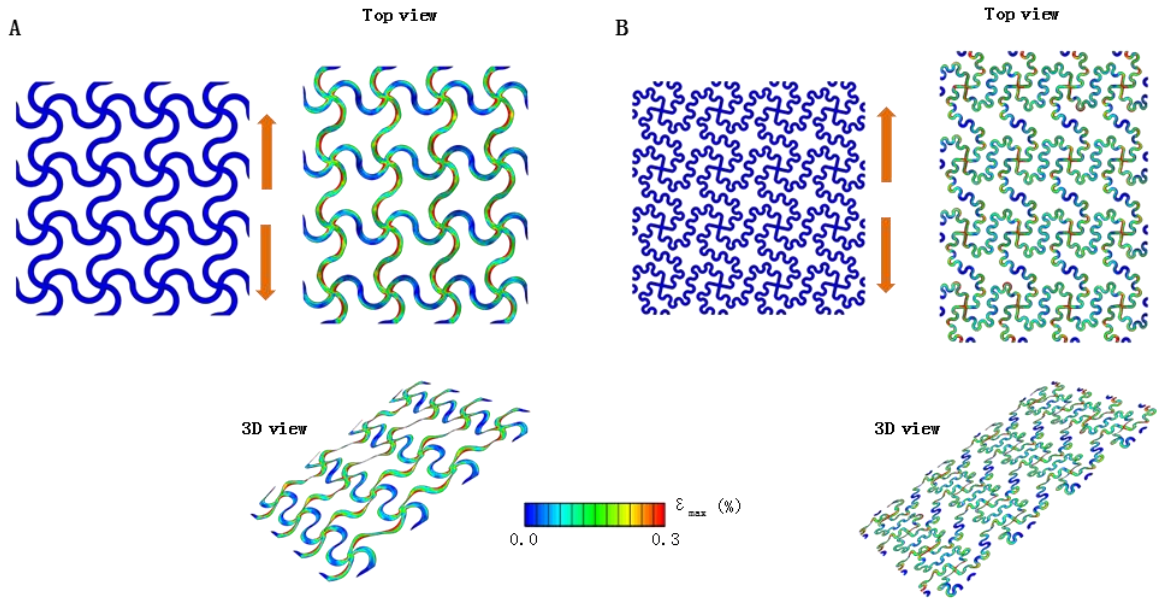

Fig. S18

3D-FEA of epidermal electrodes with self-similar serpentine mesh designs. (**A**) A traditional serpentine mesh design with a filling ratio of ~31%, and the strain distribution when the applied strain reaches the elastic stretchability (12.5%). (**B**) The self-similar serpentine mesh design with a filling ratio of ~31%, and the strain distribution when the applied strain reaches the elastic stretchability (25.0%). Both the top view and angled views of the deformed configurations are shown in the figure, indicating smaller wrinkling wavelength for the self-similar serpentine mesh design on the right.

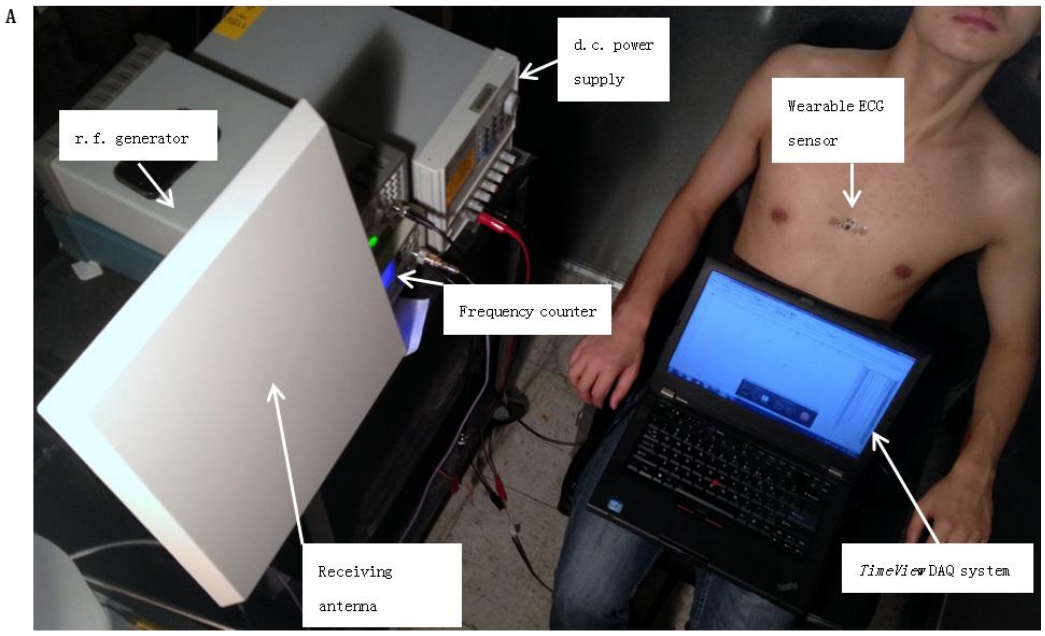

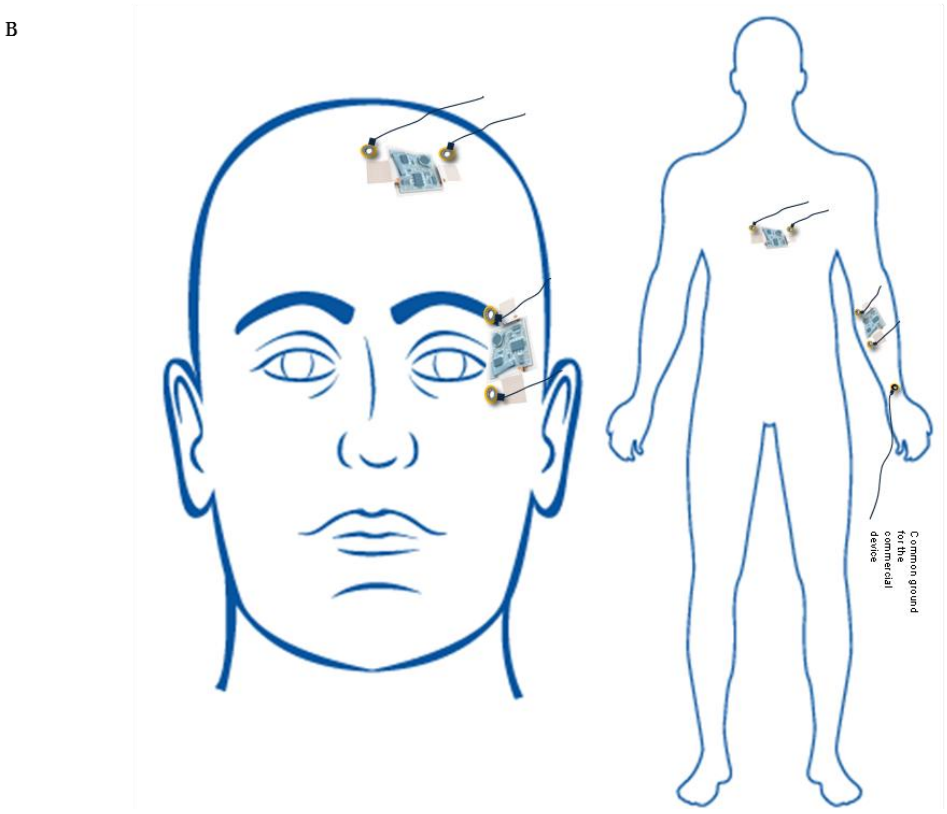

Fig. S19

Illustration of the experimental setup and measurement position on the human body. (**A**) Experimental setup to measure the ECG in a room design to eliminate background electrical noise. (**B**) Different lamination positions on the human body for measuring the electrophysiological signals.

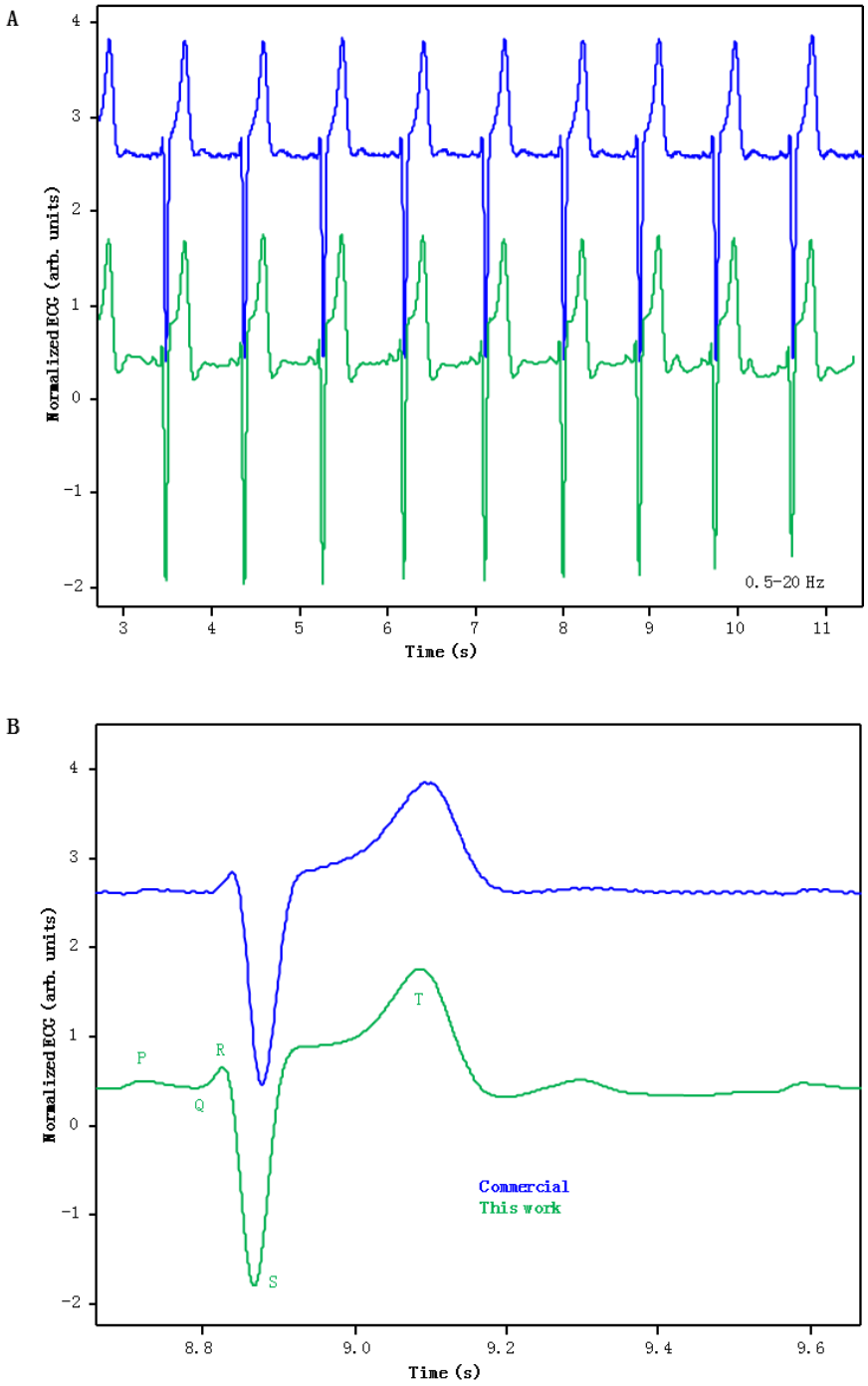

Fig. S20

Comparison of the ECG signals from this work and commercial systems. (A) ECG data acquired using a device mounted on the sternum (green) and simultaneous measurement using a wired commercial device with commercial electrodes (blue) placed next to those of the wireless system. (**B**) The expanded graph provides a detailed view that shows the expected QRS complex. The data are plotted in arbitrary units, normalized and offset in the vertical direction to facilitate comparisons.

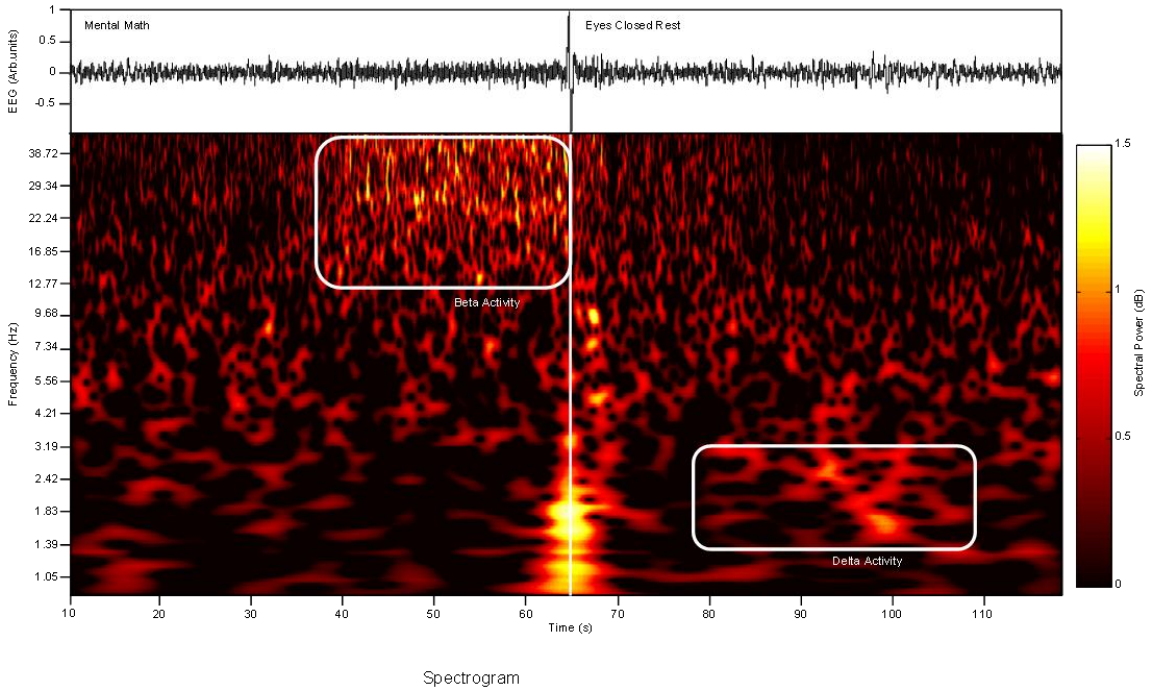

Fig. S21

A time-frequency spectrogram of the EEG computed with wavelet decomposition. EEG data from Fig. 3F, in normalized arbitrary units were decomposed using a 20 cycle wavelet transform. During mental math, an increase in high-frequency activity between 12-40 Hz (Beta band) is observed that dissipates with rest. During rest, the data show a clear peak in the lower frequency delta band that is larger than that during math.

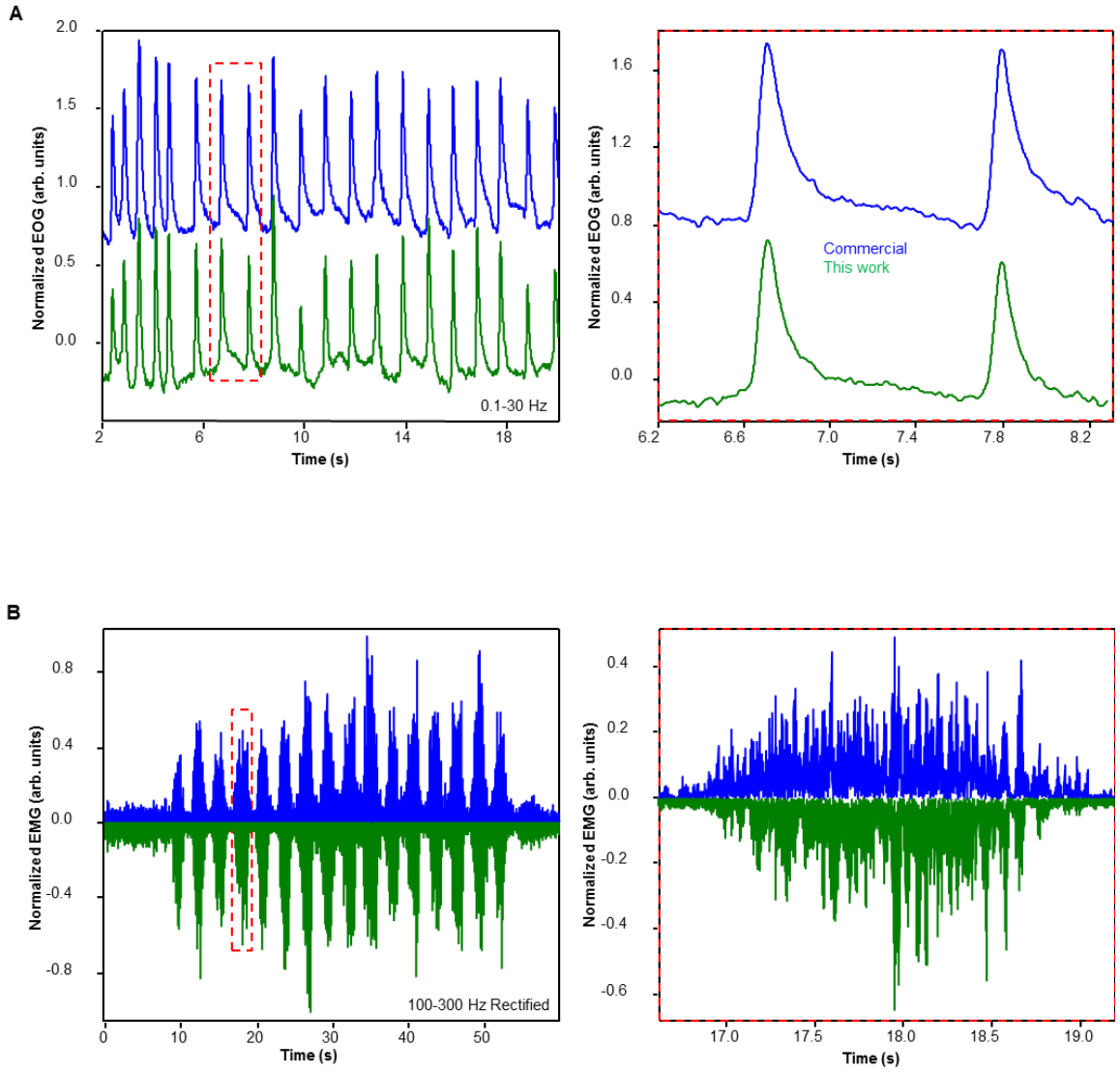

Fig. S22

EOG and EMG data with commercial device comparison. (**A**) EOG recorded at positions superior and inferior to the left eye (and slightly lateral from the left outer canthus) as the subject blinks once per second (green), and simultaneous measurement using a wired commercial device with commercial electrodes (blue) placed next to those of the wireless system. The right plot shows data during the time of two eye blinks. (**B**) EMG measured from the proximal left forearm over the flexor carpi radialis muscle during hand clenches (green), and simultaneous measurement using a wired commercial device with commercial electrodes (blue) placed next to those of the wireless system. The data from the wireless device were inverted along the vertical axis, to facilitate comparison. The right plot shows data corresponding to a single muscle contraction. The commercial system used a pair of Au plated Ag electrodes held against the head with adhesive stickers and conductive electrode gel, and a nearby ground electrode.

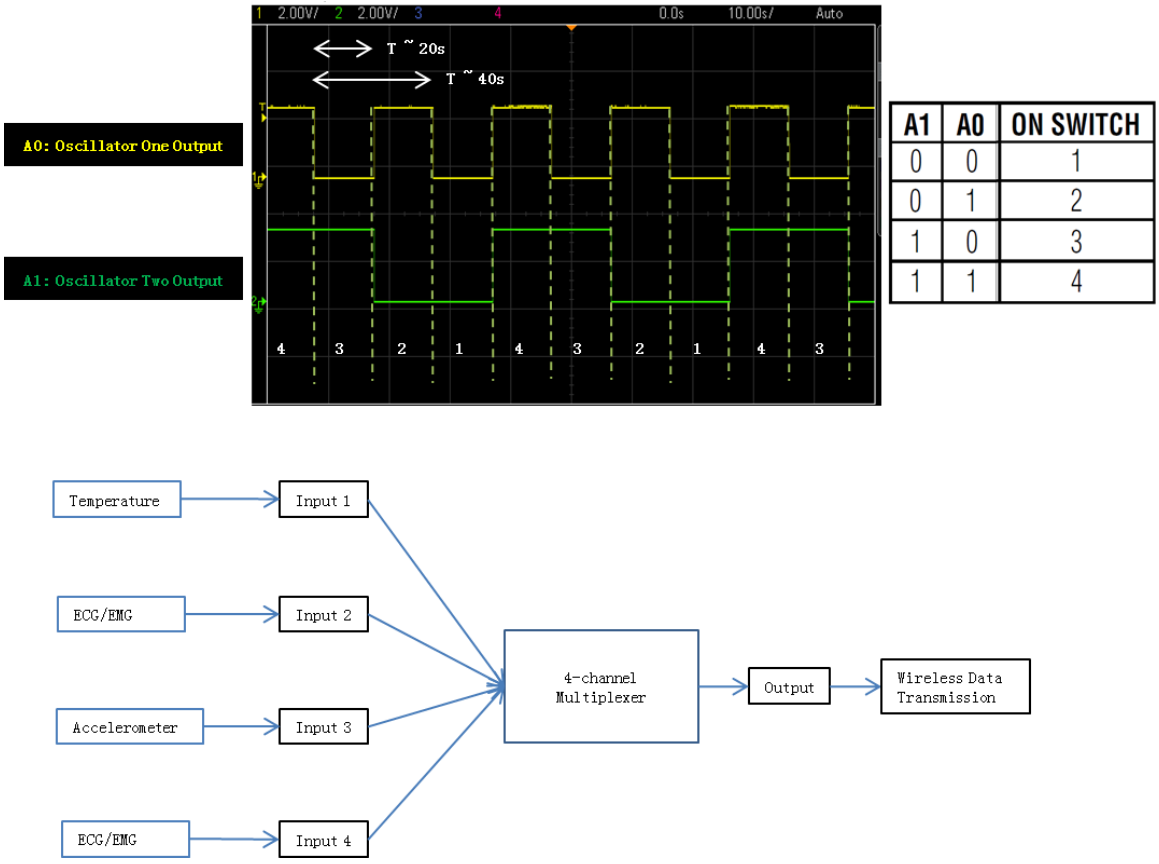

A1	A0	ON SWITCH
0	0	1
0	1	2
1	0	3
1	1	4

Fig. S23
Working principle of the multiplexer.

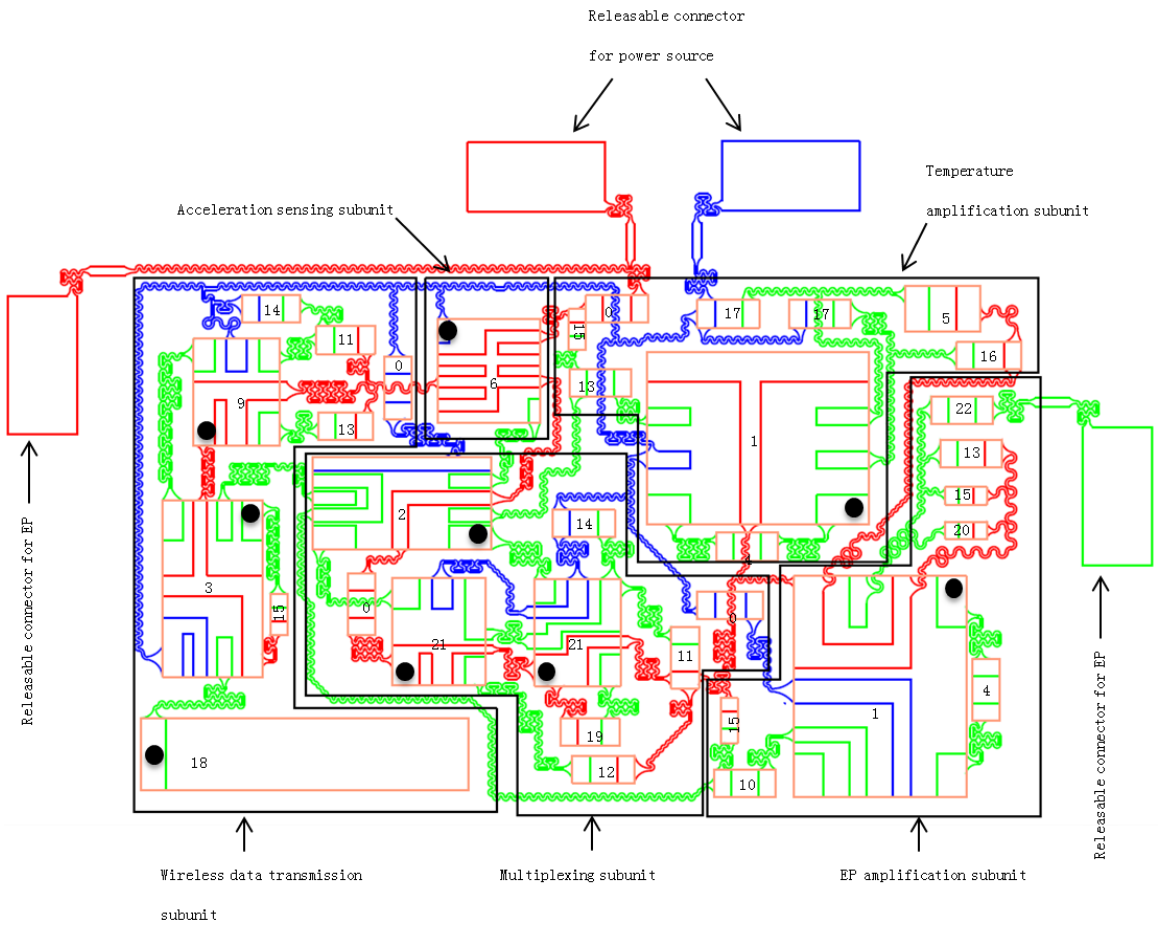

Fig. S24

The multifunctional sensor system with different parts and chip information (Table S3) labeled. Black dots indicate the number 1 pin of each individual chip.

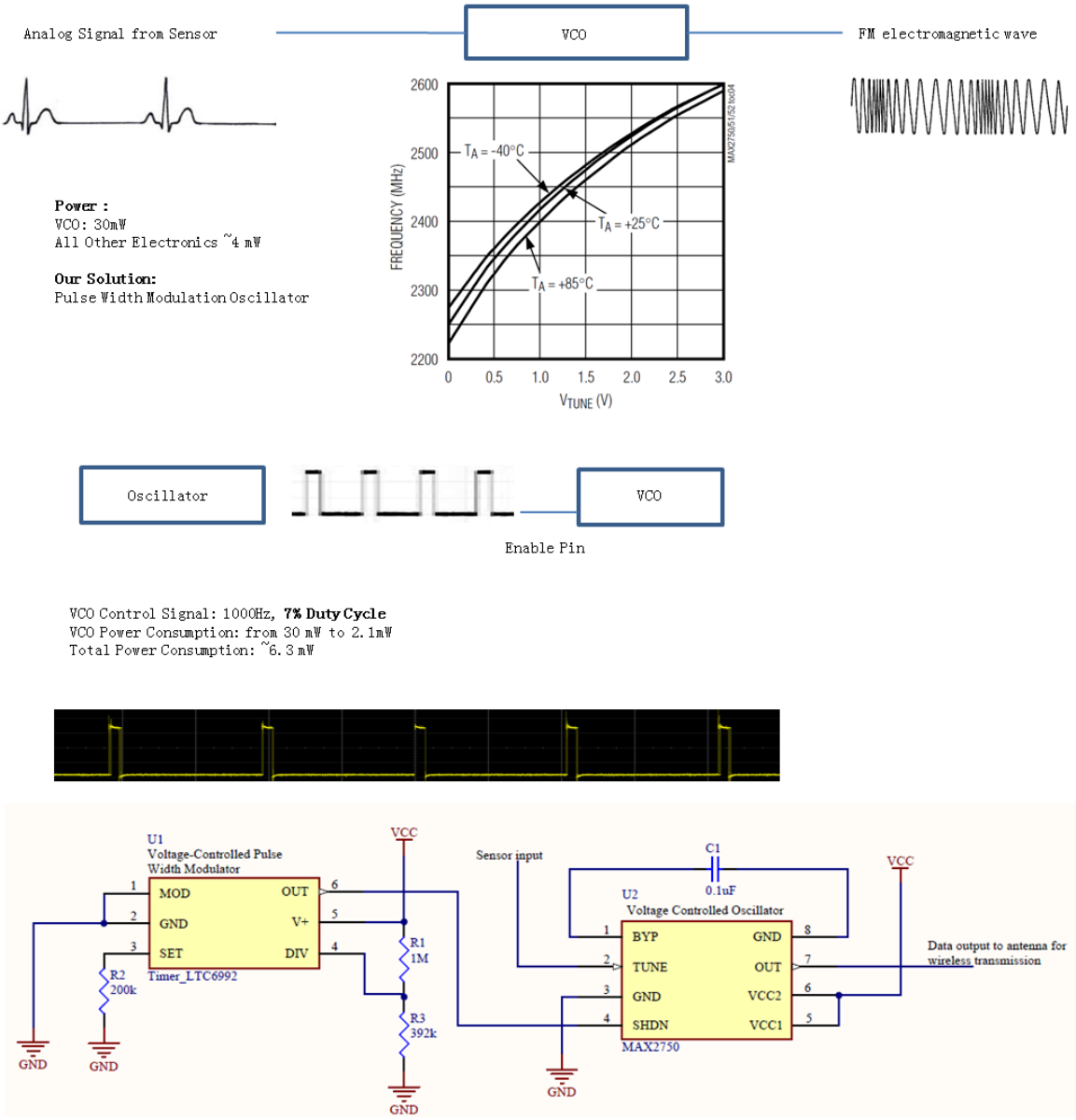

Fig. S25

Design strategy for reducing the power consumption of the voltage controlled oscillator (VCO), by adding a pulse modulator. When the VCO duty cycle is reduced to 7%, the power consumption of the entire system is about 6 mW.

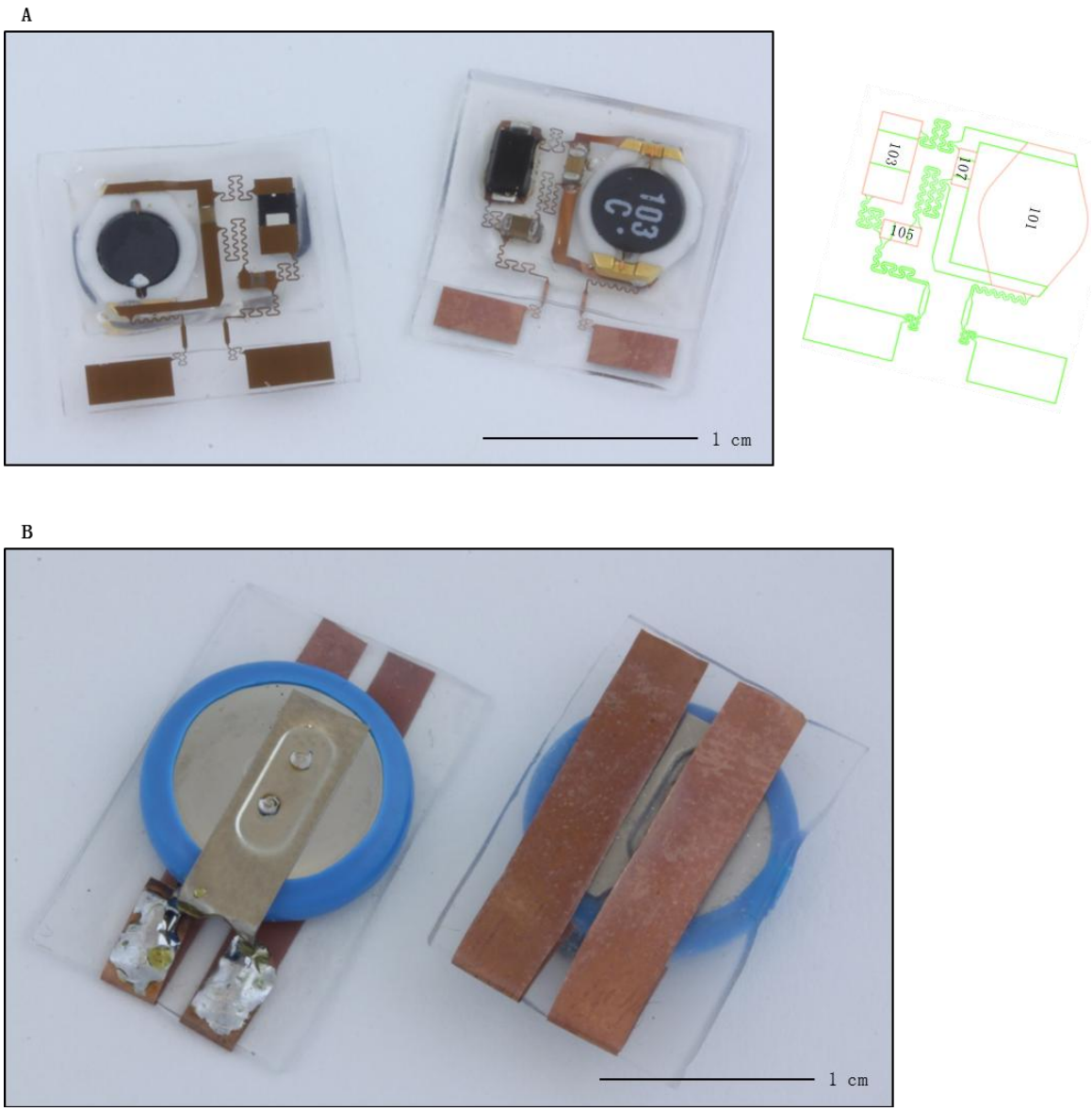

Fig. S26

Releasable power supplies for the multifunctional system. (**A**) Optical image of the NFC module from the front and back sides, and associated chip information (Table S1). (**B**) Optical image of the front and back sides of a small coin cell battery module. Both of these modules can laminate onto the power supply contact pads of the multifunctional device, to provide power for operation.

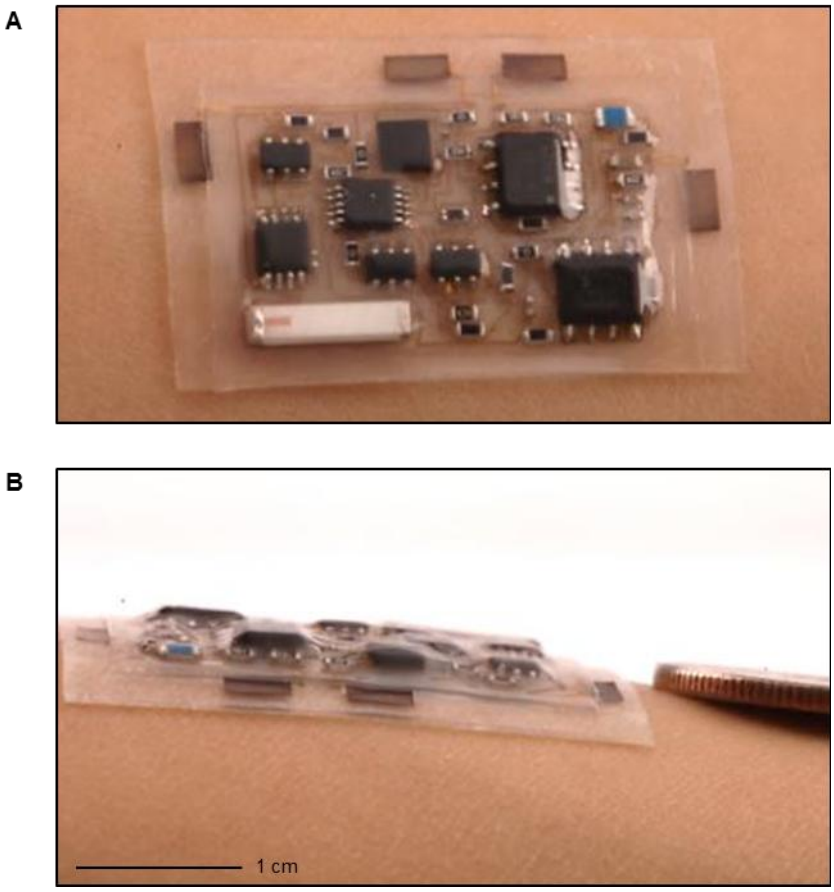

Fig. S27

Images of the device on the skin. (**A**) Top down view to show its overall footprint (1.9 x 2.9 cm^2), and (**B**) perspective view to show its overall thickness (~1 mm) with reference to a coin (US quarter).

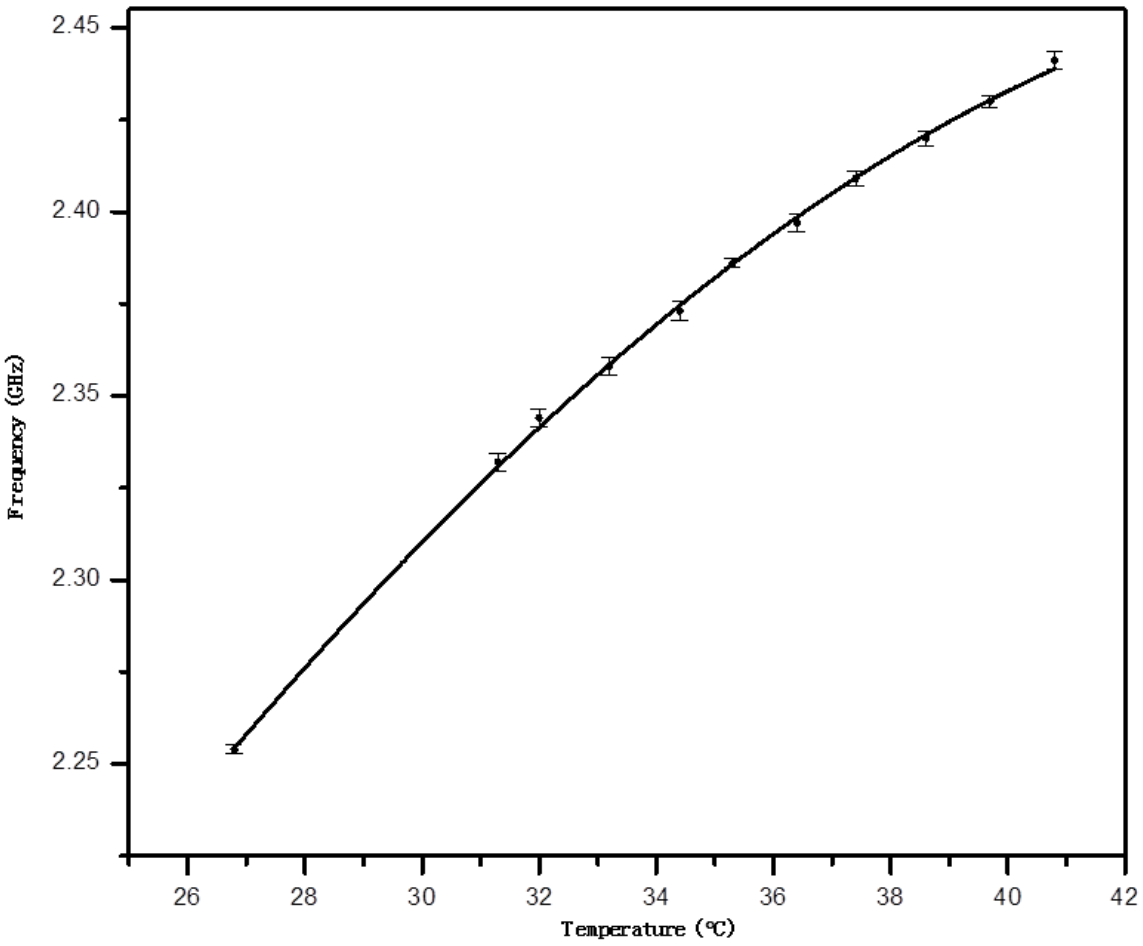

Fig. S28

Calibration curve for the temperature-frequency relationship in the multifunctional system. The error bars for each data point are from three independent measurements.

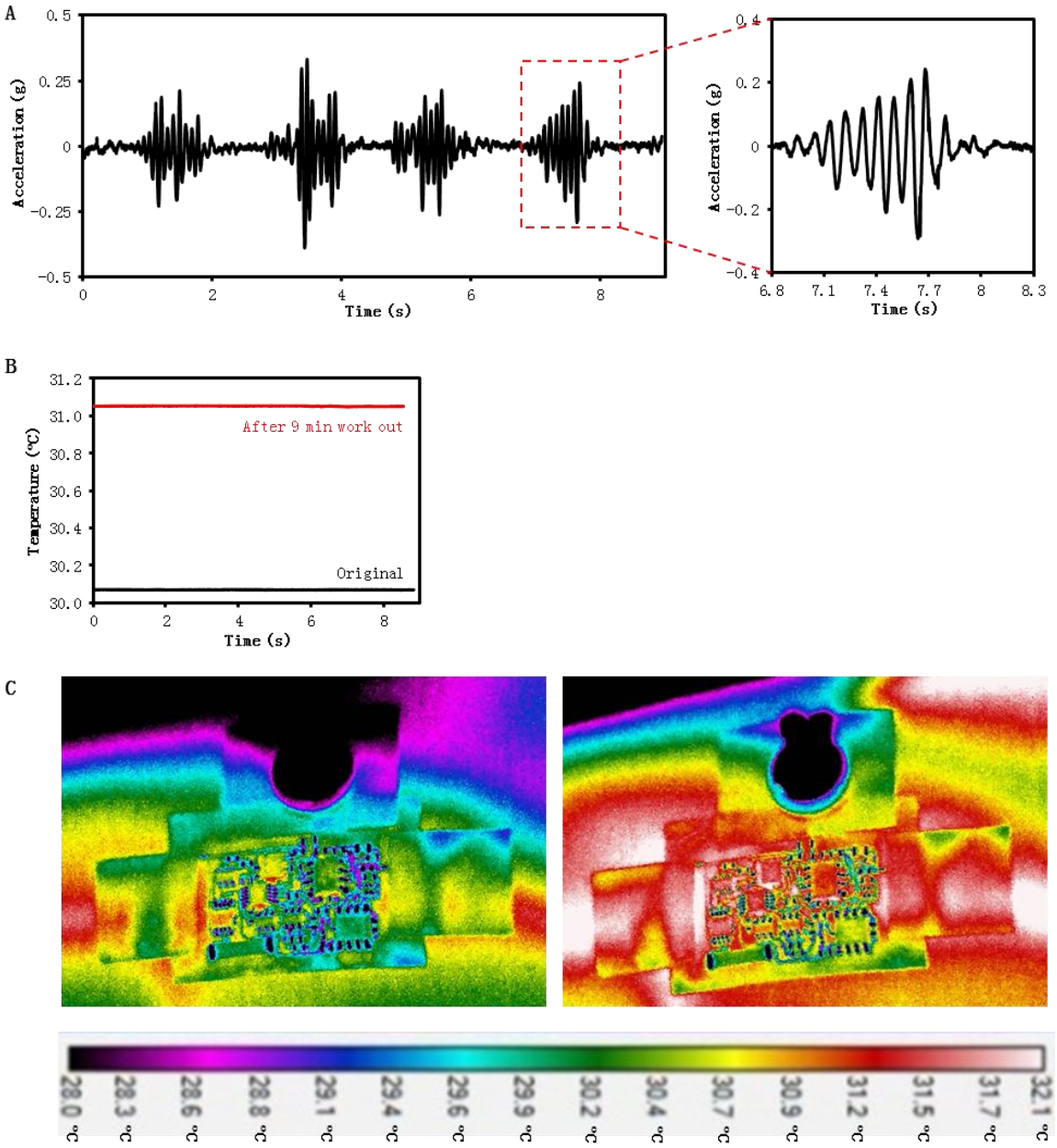

Fig. S29

Signal readouts from the multifunctional device when mounted on the forearm during periodic clinching and relaxing of the fist. (**A**) Acceleration signal and (**B**) temperature signal before and after 9 min of clinching and relaxing. (**C**) The temperature measured before (left panel) and after (right panel) this exercise, as confirmed by the commercial IR camera.

Table S1

Chip information of the ECG system.

Device number	Type	Value	Manufacturer part number
0	Jumper	0 Ω	CRCW06030000Z0EAHP
1	Operational amplifier	N/A	AD627BRZ-R7
3	Voltage controlled oscillator	N/A	MAX2750EUA+
4	Resistor	249 Ω	PAT0603E2490BST1
10	Resistor	10K Ω	ERJ-3EKF100ZV
13	Resistor	200K Ω	RG1608N-204-W-T1
18	Multilayer antenna	N/A	7488910245
101	Inductor	10 μH	27T103C
105	Capacitor	10 μF	C1608X5R1A106K
107	Capacitor	0.1 μF	C0603C104J4RACTU

Table S2

Computational model for the effective Young's modulus. The moduli for the experimental data are determined by using linear fits of the stress-strain curve in the range of [0%, 50%].

Experiment / FEA	Modulus (x)	Modulus (y)
With chip	193.80 kPa / 172.06kPa	176.88 kPa / 171.26kPa
Without chip	185.15 kPa / 166.41 kPa	166.41 kPa / 166.41 kPa
Increased percentage	4.7% / 3.4%	6.3% / 2.9%
Average	3.2%	5.5%

Table S3

Chip information for the multifunctional system.

Device number	Type	Value	Manufacturer part number
0	Jumper	0 Ω	CRCW06030000Z0EAHP
1	Operational amplifier	N/A	AD627BRZ-R7
2	IC multiplexer	N/A	MAX4734EUB+
3	Voltage controlled oscillator	N/A	MAX2750EUA+
4	Resistor	249 Ω	PAT0603E2490BST1
5	Temperature sensor	N/A	PTS080501B500RP100
6	IC accelerometer	N/A	KXTH9-2083
9	IC oscillator	N/A	LTC6992IS6-2#TRMPBF
10	Resistor	10 KΩ	ERJ-3EKF1002V
11	Resistor	392 KΩ	ERJ-3EKF3923V
12	Resistor	215 KΩ	ERA-3AEB2153V
13	Resistor	200 KΩ	RG1608N-204-W-T1
14	Resistor	1 MΩ	ERJ-3EKF1004V
15	Capacitor	0.1 µF	C0402C104K8RALTU
16	Resistor	549 Ω	ERA-3AEB5490V
17	Resistor	18 KΩ	RG1608N-183-W-T1
18	Multilayer antenna	N/A	7488910245
19	Resistor	430 KΩ	1-1879417-0
20	Capacitor	82 pF	VJ0402D820JXXAJ
21	IC oscillator	N/A	LTC6991IS6#TRMPBF
22	Capacitor	4.7 µF	C1608X5R1A475K/0.50

Movie S1

Video of the self-alignment of chips during the soldering/bonding process. Under controlled heating, the solder paste reflows and wets the serpentine metal electrodes and the contact pads on the chips. The surface tension causes motion that maximizes the contact area to the metal electrodes underneath, thereby self-aligning the chips.

Movie S2

This video shows an ECG device during operation. This device has three basic functions: wireless power transfer, electrophysiological potential sensing and wireless data transmission to an external receiving system. When the inductive coil is placed near the secondary coil in the device, the ECG signal from the chest of a test subject was amplified, filtered and wirelessly transmitted to a receiver. The resulting data appears in real time on the computer screen, as it is recorded. The drifting baseline of the signal in the first few seconds is because of a capacitor connected in series in the circuit.

References and Notes

1. D. H. Kim, N. Lu, R. Ma, Y. S. Kim, R. H. Kim, S. Wang, J. Wu, S. M. Won, H. Tao, A. Islam, K. J. Yu, T. I. Kim, R. Chowdhury, M. Ying, L. Xu, M. Li, H. J. Chung, H. Keum, M. McCormick, P. Liu, Y. W. Zhang, F. G. Omenetto, Y. Huang, T. Coleman, J. A. Rogers, Epidermal electronics. *Science* **333**, 838–843 (2011). doi:10.1126/science.1206157

2. J.-W. Jeong, W. H. Yeo, A. Akhtar, J. J. Norton, Y. J. Kwack, S. Li, S. Y. Jung, Y. Su, W. Lee, J. Xia, H. Cheng, Y. Huang, W. S. Choi, T. Bretl, J. A. Rogers, Materials and optimized designs for human-machine interfaces via epidermal electronics. *Adv. Mater.* **25**, 6839–6846 (2013). doi:10.1002/adma.201301921 Medline

3. M. Kaltenbrunner, T. Sekitani, J. Reeder, T. Yokota, K. Kuribara, T. Tokuhara, M. Drack, R. Schwödiauer, I. Graz, S. Bauer-Gogonea, S. Bauer, T. Someya, An ultra-lightweight design for imperceptible plastic electronics. *Nature* **499**, 458–463 (2013). doi:10.1038/nature12314 Medline

4. M. S. White, M. Kaltenbrunner, E. D. Głowacki, K. Gutnichenko, G. Kettlgruber, I. Graz, S. Aazou, C. Ulbricht, D. A. M. Egbe, M. C. Miron, Z. Major, M. C. Scharber, T. Sekitani, T. Someya, S. Bauer, N. S. Sariciftci, Ultrathin, highly flexible and stretchable PLEDs. *Nat. Photonics* **7**, 811–816 (2013). doi:10.1038/nphoton.2013.188

5. M. S. Mannoor, H. Tao, J. D. Clayton, A. Sengupta, D. L. Kaplan, R. R. Naik, N. Verma, F. G. Omenetto, M. C. McAlpine, Graphene-based wireless bacteria detection on tooth enamel. *Nat. Commun.* **3**, 763 (2012). doi:10.1038/ncomms1767 Medline

6. J. A. Rogers, M. G. Lagally, R. G. Nuzzo, Synthesis, assembly and applications of semiconductor nanomembranes. *Nature* **477**, 45–53 (2011). doi:10.1038/nature10381 Medline

7. C. F. Pan, L. Dong, G. Zhu, S. Niu, R. Yu, Q. Yang, Y. Liu, Z. L. Wang, High-resolution electroluminescent imaging of pressure distribution using a piezoelectric nanowire LED array. *Nat. Photonics* **7**, 752–758 (2013). doi:10.1038/nphoton.2013.191

8. C. Wang, D. Hwang, Z. Yu, K. Takei, J. Park, T. Chen, B. Ma, A. Javey, User-interactive electronic skin for instantaneous pressure visualization. *Nat. Mater.* **12**, 899–904 (2013). doi:10.1038/nmat3711 Medline

9. S. C. B. Mannsfeld, B. C. Tee, R. M. Stoltenberg, C. V. Chen, S. Barman, B. V. Muir, A. N. Sokolov, C. Reese, Z. Bao, Highly sensitive flexible pressure sensors with microstructured rubber dielectric layers. *Nat. Mater.* **9**, 859–864 (2010). doi:10.1038/nmat2834 Medline

10. D. J. Lipomi, M. Vosgueritchian, B. C. Tee, S. L. Hellstrom, J. A. Lee, C. H. Fox, Z. Bao, Skin-like pressure and strain sensors based on transparent elastic films of carbon nanotubes. *Nat. Nanotechnol.* **6**, 788–792 (2011). doi:10.1038/nnano.2011.184 Medline

11. T. Sekitani, T. Someya, Stretchable organic integrated circuits for large-area electronic skin surfaces. *MRS Bull.* **37**, 236–245 (2012). doi:10.1557/mrs.2012.42

12. G. Schwartz, B. C. Tee, J. Mei, A. L. Appleton, H. Kim, H. Wang, Z. Bao, Flexible polymer transistors with high pressure sensitivity for application in electronic skin and health monitoring. *Nat. Commun.* **4**, 1859 (2013). doi:10.1038/ncomms2832 Medline

13. C. Keplinger, J. Y. Sun, C. C. Foo, P. Rothemund, G. M. Whitesides, Z. Suo, Stretchable, transparent, ionic conductors. *Science* **341**, 984–987 (2013). doi:10.1126/science.1240228 Medline

14. M. Kubo, X. Li, C. Kim, M. Hashimoto, B. J. Wiley, D. Ham, G. M. Whitesides, Stretchable microfluidic radiofrequency antennas. *Adv. Mater.* **22**, 2749–2752 (2010). doi:10.1002/adma.200904201 Medline

15. E. Palleau, S. Reece, S. C. Desai, M. E. Smith, M. D. Dickey, Self-healing stretchable wires for reconfigurable circuit wiring and 3D microfluidics. *Adv. Mater.* **25**, 1589–1592 (2013). doi:10.1002/adma.201203921 Medline

16. D. M. Vogt, Y. L. Park, R. J. Wood, Design and Characterization of a Soft Multi-Axis Force Sensor Using Embedded Microfluidic Channels. *IEEE Sens. J.* **13**, 4056–4064 (2013). doi:10.1109/JSEN.2013.2272320

17. S. Wagner, S. Bauer, Materials for stretchable electronics. *MRS Bull.* **37**, 207–213 (2012). doi:10.1557/mrs.2012.37

18. T. Sterken, J. Vanfleteren, T. Torfs, M. O. de Beeck, F. Bossuyt, C. Van Hoof, Ultra-Thin Chip Package (UTCP) and stretchable circuit technologies for wearable ECG system. *Conf. Proc. IEEE Eng. Med. Biol. Soc.* **2011**, 6886–6889 (2011). Medline

19. F. Axisa, D. Brosteaux, E. De Leersnyder, F. Bossuyt, J. Vanfleteren, B. Hermans, R. Puers, *Conf. Proc. IEEE Eng. Med. Biol. Soc.* **2011**, 5687–5690 (2007). doi:10.1109/IEMBS.2007.4353637

20. M. Gonzalez, B. Vandevelde, W. Christiaens, Y.-Y. Hsu, F. Iker, F. Bossuyt, J. Vanfleteren, O. Sluis, P. H. M. Timmermans, Design and implementation of flexible and stretchable systems. *Microelectron. Reliab.* **51**, 1069–1076 (2011). doi:10.1016/j.microrel.2011.03.012

21. H. Vandeparre, Q. Liu, I. R. Minev, Z. Suo, S. P. Lacour, Localization of folds and cracks in thin metal films coated on flexible elastomer foams. *Adv. Mater.* **25**, 3117–3121 (2013). doi:10.1002/adma.201300587 Medline

22. A. Romeo, Q. H. Liu, Z. G. Suo, S. P. Lacour, Elastomeric substrates with embedded stiff platforms for stretchable electronics. *Appl. Phys. Lett.* **102**, 131904 (2013). doi:10.1063/1.4799653

23. S. P. Lacour, S. Wagner, R. J. Narayan, T. Li, Z. G. Suo, Stiff subcircuit islands of diamondlike carbon for stretchable electronics. *J. Appl. Phys.* **100**, 014913 (2006). doi:10.1063/1.2210170

24. Y. Lee, B. Giridhar, Z. Foo, D. Sylvester, D. B. Blaauw, A Sub-nW multi-stage temperature compensated timer for ultra-low-power sensor nodes. *IEEE J. Solid-State Circuits* **48**, 2511–2521 (2013). doi:10.1109/JSSC.2013.2275660

25. Y. Lee, S. Bang, I. Lee, Y. Kim, G. Kim, M. H. Ghaed, P. Pannuto, P. Dutta, D. Sylvester, D. Blaauw, A modular 1 mm^3 die-stacked sensing platform with low power I^2C inter-die

communication and multi-modal energy harvesting. *IEEE J. Solid-State Circuits* **48**, 229–243 (2013). doi:10.1109/JSSC.2012.2221233

26. Y. Sun, H. Luo, S. K. Das, A trust-based framework for fault-tolerant data aggregation in wireless multimedia sensor networks. *IEEE Trans. Depend. Secure Comput.* **9**, 785–797 (2012). doi:10.1109/TDSC.2012.68

27. E. Y. Chow, M. M. Morris, P. P. Irazoqui, Implantable RF medical devices: The benefits of high-speed communication and much greater communication distances in biomedical applications. *IEEE Microw. Mag.* **14**, 64–73 (2013). doi:10.1109/MMM.2013.2248586

28. S. Kim, J. S. Ho, A. S. Y. Poon, Midfield wireless powering of subwavelength autonomous devices. *Phys. Rev. Lett.* **110**, 203905 (2013). doi:10.1103/PhysRevLett.110.203905

29. S. J. Thomas, R. R. Harrison, A. Leonardo, M. S. Reynolds, A battery-free multichannel digital neural/EMG telemetry system for flying insects. *IEEE Trans. Biomed. Circuit Syst.* **6**, 424–436 (2012). doi:10.1109/TBCAS.2012.2222881

30. Y. Sun, W. M. Choi, H. Jiang, Y. Y. Huang, J. A. Rogers, Controlled buckling of semiconductor nanoribbons for stretchable electronics. *Nat. Nanotechnol.* **1**, 201–207 (2006). doi:10.1038/nnano.2006.131 Medline

31. V. Medina, J. M. Clochesy, A. Omery, Comparison of electrode site preparation techniques. *Heart Lung* **18**, 456–460 (1989). Medline